RESEARCH ARTICLE

Dual Loop PI^{m}PI^n Control for an Aileron Positioning

ALESSANDRO DE GASPARI[ID] AND PAOLO MANTEGAZZA[ID]

Department of Aerospace Science and Technology, Politecnico di Milano, 20156 Milan, Italy

Corresponding author: Alessandro De Gaspari (alessandro.degaspari@polimi.it)

ABSTRACT Aircraft control surfaces are subjected to uncertain design parameters and time–varying external disturbances related to aerodynamic loads. This paper presents a control formulation for their positioning based on a velocity/position dual loop, embedding an arbitrary order of integral actions determined through a simple linear design. The adoption of an appropriate high order integration aims to compensate for external disturbances, modeling uncertainties and the impact of some nonlinearities. Relevant design and implementation issues were also described, including windup mitigation and the use of an observer to compensate for out–of–band disturbances. After a numerical model validation comprising a Monte Carlo assessment of the combined uncertainties, the controller was verified experimentally. The test bench was made up of the aileron of a wind tunnel model, driven by an electric motor through a mildly tensioned timing belt transmission. The results of a significant test set are provided to demonstrate the effectiveness of such a controller against noteworthy design uncertainties, such as sliding friction, sensor failure, free play due to inadequate belt tension, and approximate design parameters.

INDEX TERMS Design uncertainty, disturbance rejection, high order integration, nonlinearity, real–time control, servo controller.

NOMENCLATURE

Δt	sampling time.
ω	motor velocity (rad s^{-1}).
ω_0, f_0	generic design bandwidths (rad s^{-1}, Hz).
ω_c	commanded control surface velocity (rad s^{-1}).
ω_f	control surface velocity feed–forward (rad s^{-1}).
ω_i	current drive bandwidth (rad s^{-1}).
ω_r	reference motor velocity (rad s^{-1}).
ω_s	control surface velocity (rad s^{-1}).
τ	toothed belt transmission ratio θ/θ_s.
θ	motor rotation (rad).
θ_c	commanded control surface rotation (rad).
θ_r	reference control surface reference rotation (rad).
θ_s	control surface rotation (rad).
C	motor damping (N m s).
J	total inertia (kg m^2).
J_a	control surface inertia (kg m^2).
J_m	motor inertia (kg m^2).
K	motor stiffness (N m).
k_P^p	proportional gain of the position loop, equal to $k_{I,0}^p$.
k_P^v	proportional gain of the velocity loop, equal to $k_{I,0}^v$.
$k_{I,i}^p$	i–th order integral gain of the position loop.
$k_{I,i}^v$	i–th order integral gain of the velocity loop.
m	maximum integration order for the velocity loop.
n	maximum integration order for the position loop.
s	Laplace variable.
s_f	dividing scale factor to achieve a 3 dB bandwidth at ω_0.
t	time (s).
T_c	commanded motor torque (N m).
T_d	torque disturbances, as reduced to the motor shaft (N m).
T_f	torque feed–forward (N m).
T_i	current drive output torque (N m).
T_m	resulting motor torque command (N m).
u	generic control output.

$y, \dot{y}$	generic sensed feedback input and its time rate.
y_c	generic command input.
"motor"	designation used for the motor + harmonic speed reducer.

I. INTRODUCTION

Feedback control systems used to command aircraft control surfaces operate under highly variable flight conditions. Furthermore, they must withstand a wide range of static and dynamic loads owing to flight maneuvers and gusts/turbulence [1], [2], whereas control surfaces are required to change position while remaining insensitive to any load variation. Moreover, regardless of their driving physics, they are subject to multiple saturations, that is, position, velocity, and force/torque stall. All these must be duly scaled in wind tunnel models, whereas an actuating device can differ from its full–scale counterpart. This is the case when electro–hydraulic actuators (EHAs) cannot be adequately miniaturized or the required hydraulic power is not easily available. Therefore, they must be replaced by miniature electrical motors, as is the case in this study.

Within this framework, single loop proportional–integral–derivative (PID) controllers [3], [4] are easily designed, but cannot satisfy the velocity constraints and incorporate poor capabilities to compensate for more than piecewise constant external disturbances; therefore, they can be effective only over a limited range of scaled flight conditions and might require some gain scheduling. Nonetheless, once a working initial design setup is available, it is often possible to improve its performance through a variety of on–site auto–tuning methods commonly adopted in industrial applications [5], [6]. Furthermore, as can be seen in the literature, there is a persisting interest in their use and continued work aimed at getting the most out of them by adopting more effective design approaches such as citing only a few: adaptive [7], [8], [9], [10], optimal robust [11], [12], [13], fuzzy [14], [15], neural net–based [16], [17], [18], and online optimization [19], [20].

Because this paper presents the idea of extending the PID terms with integrals of order greater than one in positioning controllers, it should be interesting to note that the transfer function from a position, say y, to the motor drive input, say u, of many existing dual loop PID–PID controllers, adopting a single integration in each loop, is already an often unnoticed outcome equivalent to single loop PI^{2}Ds and PI^{2}s controllers, adopting a double integration (I^2). To verify such a matching, the following terms for the single loop PI^{2}D are defined: derivative gain k_d, proportional gain k_p, single k_{i1} and double k_{i2} integral gains, whereas k_D^p, for the derivative of y, has to be added to the terms already available in the dual loop PI^{m}PI^n nomenclature. Then, combining a PI speed loop with a PID position loop, after assuming that the two loops are commanded only through their integral terms, the resulting PI–PID controller will provide $u = -\left(k_P^v + k_{I,1}^v/s\right) \cdot \dot{y} - k_{I,1}^v/s \left(k_D^p s + k_P^p + k_{I,1}^p/s\right) \cdot y$, such that,

being $\dot{y} = s\, y$, $u = -(k_P^v s^3 + k_{I,1}^v \left(1 + k_D^p\right) s^2 + k_{I,1}^v k_P^p s + k_{I,1}^v k_{I,1}^p)/s^2 \cdot y$, which is clearly a match of its single loop PI^{2}D counterpart, that is, $u = -(k_d s + k_p + k_{i1}/s + k_{i2}/s^2) \cdot y = -(k_d s^3 + k_p s^2 + k_{i1} s + k_{i2})/s^2 \cdot y$.

Then, after remarking that a plainer PI–PI formulation, that is, with $k_D^p = 0$, will provide a transfer function with the same structure, the correspondence for a somewhat simpler single loop PI^2 scheme will follow by merely setting $k_0^v = k_d = 0$.

What has just been addressed above, mated to the available tools for a highly effective design and fine tuning of any single loop PID, has likely shadowed the need to use truly high order integrals, so that adoption has been rarer.

Nonetheless, in the literature, it is possible to find instances of the use of up to double integrals, either in the form of a dual loop PI^{2}D controller [21] or as a single loop PI^2 controller [22].

In relation to Linear Quadratic Tracking (LQT) problems, [23] reported a classification of possible improved solutions based on arbitrary order PI^{m}D^{n-1} controllers implemented through both single and dual loop schemes, with explicit formulae up to I^2 terms.

There are also instances of PI^2 industrial controllers. For example, [24] features a single loop speed control that can be cast as $G_p \left(1 + \Omega_{stop}/s\right)^2$, G_p being a user–assigned loop gain and Ω_{stop} the so–called integration stop frequency.

It is worth noting that among the above referenced papers, only [22] explicitly considers possible windups through the conditional sliding mode integration of [25]. However, considering that the use of high order integrators may significantly worsen the effects of saturated controls, the adoption of windup mitigation should be unevoidable.

The use of a dual loop with more than two per–loop integral terms is considered here as a possible alternative to the dual loop PID controllers based on an unfalsified and Quantitative Feedback Theory (QFT) formulation [26], [27], previously installed on wind tunnel models, with the objective of obtaining equal/better performances through a significantly simpler design method. Such a commitment aims to make it possible to safely redesign at varying dynamic pressures on the fly and within any sampled control cycle, possibly avoiding them altogether. A solution that was not viable with the previously mentioned formulations requiring interpolated scheduling over a set of off–line designs parameterized against the dynamic pressure.

Consequently, the proposed dual loop architecture consists of an inner loop acting on the rotational velocity of the motor and an outer loop acting on the position of the control surface. Both the inner and outer loops are structured as a proportional term plus the sum of m and n integral terms, respectively, addressed by the notation PI^m and PI^n, simply synthesized as PI^{m}PI^n in the following, where m and n are the number of integrals and the maximum order of integration in each loop, respectively. Within such a framework, an anti–windup scheme and out–of–band disturbance compensation are unified in the formulation of simply designed observers, thus leading to a system capable of effectively mimicking the

scaled technological limitations related to actual EHAs and electro–mechanical actuators (EMAs) [28].

Then, high order integrals combined with an appropriate set of closed loop poles can ensure proper shaping of the open loop transfer function, making it possible to guarantee adequate margins against design uncertainties and a strong rejection of time–varying external disturbances, for example, dynamic pressure–dependent aerodynamic loads. That being so, and adopting an appropriate pole assignment for the previously mentioned observers, the entire controller design will be carried out using simple algebraic formulae and the sole knowledge of the inertia of the motor–transmission–aileron, thus making it viable any needed on the fly rescheduling hinted at before. Nonetheless, because of the discarded significant harmonic motor sliding stiction/friction, compliance, and free–play in the slightly tensioned toothed belt transmission to be described later, the above design procedure will be first validated through a nonlinear, middle–fidelity model and an extensive set of tests. The ability to tolerate the above nonlinearities is of key importance because they are difficult to quantify and can vary significantly during their operational life [29].

The aforementioned experimental validation of the proposed control strategy and related design approach was carried out by applying the proposed controller to the positioning servo of the aileron of an aeroservoelastic wind tunnel model, previously servoed with [26] and [27]. Such a model is related to research on an advanced Green Regional Aircraft (GRA), which was based at the Department of Aerospace Science and Technology of Politecnico di Milano, within the cooperative EU funded project named GLAMOUR (Gust Load Alleviation techniques assessment on wind tUnnel MOdel of advanced Regional aircraft), a framework of the Clean Sky Joint Technology Initiative [30].

This article summarizes the theoretical and practical aspects aimed at developing a new controller design method, a description of its digital implementation and the numerical and experimental results obtained during the test campaign. The reminder of this paper is organized as follows. The servo controller formulation, detailed in Section II, leads to the proposed design equations (subsection II-C), implementation of the complete dual loop controller (subsections II-D and II-E), and their digital conversion (subsection II-F). Section III describes the selected aileron test bench and the controller design applied to it, and Section IV introduces the hardware and real–time environment of the test rig setup. Finally, Section V describes the two main phases of the numerical and experimental tests. The first phase consists of the study of the uncertainty propagation through Monte Carlo simulations (subsection V-A), followed by numerical model tuning (subsection V-B) and numerical/experimental correlations (subsection V-C). The second phase presents some experimental results obtained by varying the integration order and for different backlash values induced by the mechanical transmission, with a specific focus on the importance of using a disturbance observer in combination with high order

integrators (subsection V-D). The last subsection (V-E) was used to assess the controller performance against significant changes in the experimental test setup.

II. PI^{m}PI^n SERVO–CONTROL SYSTEMS

The positioning controller developed in this study is related to the aileron test bench described in Section III. As hinted at in the introduction its newness content is related to the adoption of a PI$^m(\omega)$–PI$^n(\theta)$ dual loop structure based on high order integrals, up to m and n respectively, as depicted in Fig. 1.
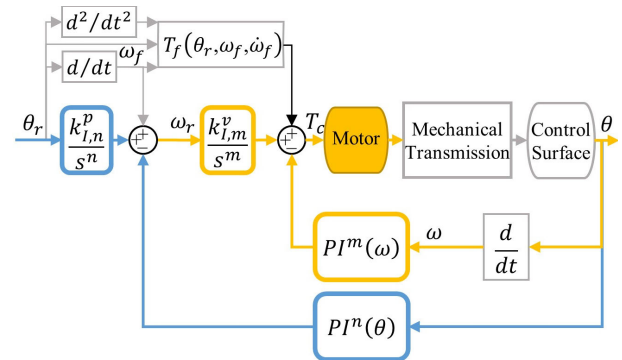

FIGURE 1. Simplified dual loop design scheme.

The servo is designed using a dual loop velocity–rotation control owing to the need to independently consider the constraint imposed on T_c, ω and θ, for example, their saturations required to emulate the technological limitations of actual fully electric or electro–hydraulic actuators installed on aircraft.

First, the motor–control surface set–up was modeled as a single rigid degree–of–freedom system, assuming that the mechanical transmission connecting the motor to the control surface was sufficiently stiff to ensure an acceptable separation of its lowest vibration mode frequency with respect to any foreseeable control bandwidth. This equivalent single–degree–of–freedom system is simply dubbed the motor, whose state $\{\theta \ \omega\}^T$, is related to the output shaft of the harmonic speed reducer. This simplification is exploited to define a simple continuous–time design procedure. In Section V, through an improved simulation model and some experimental tests, it is shown that this simply designed controller can provide good performance, despite being designed on the basis of partial knowledge of its mechanical properties and neglecting significant nonlinearities, such as saturations, sliding friction, and free–plays.

Therefore, the simplified equations of motion of the motor can be expressed in the Laplace transform domain as follows:

$$\left(Js + C + \frac{K}{s}\right)\omega = T_c + T_d \tag{1a}$$

$$\left(Js^2 + Cs + K\right)\theta = T_c + T_d \tag{1b}$$

where $\omega = s\theta$ and, lumping the transmission mass to the motor and aileron, J is the equivalent total moment of inertia, including both the motor inertia J_m and controlled

surface inertia J_a, according to the transport equation $J = J_m + J_a/\tau^2$. It should be noted that J, C, K can also comprise contributions related to a quasi steady aerodynamic approximation of the control surface hinge moment associated with the flow, thus depending on the free–stream dynamic pressure. As shown in (2), T_c is first servoed to the reference velocity ω_r in the inner loop, which is then commanded by the position error $(\theta_r - \theta)$ coming from the outer loop. The velocity loop was based on m integrals and a proportional term, whereas the position loop was based on n integrals and a proportional term.

The related equations are:

$$T_c = \frac{k_{I,m}^v}{s^m}(\omega_r - \omega) - \sum_{i=0}^{m-1} \frac{k_{I,i}^v}{s^i}\omega + T_f \tag{2a}$$

$$= \frac{k_{I,m}^v}{s^m}\omega_r - \sum_{i=0}^{m} \frac{k_{I,i}^v}{s^i}\omega + T_f = \frac{k_{I,m}^v}{s^m}\omega_r - PI^m(\omega) + T_f \tag{2b}$$

$$\omega_r = \frac{k_{I,n}^p}{s^n}(\theta_r - \theta) - \sum_{j=0}^{n-1} \frac{k_{I,j}^p}{s^j}\theta + \omega_f \tag{2c}$$

$$= \frac{k_{I,n}^p}{s^n}\theta_r - \sum_{j=0}^{n} \frac{k_{I,j}^p}{s^j}\theta + \omega_f = \frac{k_{I,n}^p}{s^n}\theta_r - PI^n(\theta) + \omega_f \tag{2d}$$

where, trivial but helpful remark, the index 0 implies:

$$k_{I,0}^p = k_P^p \quad \text{and} \quad k_{I,0}^v = k_P^v, \tag{3}$$

that is, a proportional–only control is the one with m and/or n equal to 0. The sensed variable, through an incremental encoder, is θ, ω being obtained by numerical differentiation with a time step varying in relation to the motor rotational speed. Furthermore, ω_f provides a velocity feed–forward aimed at expediting θ_r tracking. The terms k_P^v and $\frac{k_{I,1}^v}{s}$ are the usually defined proportional and integral gains for the velocity loop, respectively, which are coupled to any linear damping and stiffness reduced to the motor shaft. The desired velocity ω_r actuates only the highest order m of the integral gains in (2a), thus providing a closed loop transfer function without zeros. Similarly, the desired rotation θ_r affects only the highest integral gain n in (2c) [31]. It is additionally assumed that the bandwidth of the torque controller, that is the current drive loop, will be in the kHz range and requires no modeling, thus making it possible to write the simplified closed loop response equations detailed in the following sections.

A. VELOCITY LOOP

After substituting (2a) into (1a), we have:

$$\left[Js^{m+1} + \left(C + k_P^v\right)s^m + (K + k_{I,1}^v)s^{m-1} + \sum_{i=2}^{m} k_{I,i}^v s^{m-i} \right]\omega = k_{I,m}^v \omega_r + T_f s^m + T_d s^m \tag{4}$$

Exploiting the values of θ_r, ω_f and $\dot\omega_f$, to be provided by an input shaping filter, the optional feed–forward T_f is defined as $T_f = T_{fc} + J_f\dot\omega_f + C_f\omega_f + K_f\theta_r$, where T_{fc} is a constant feed–forward, J_f, C_f and K_f are the design parameters. Hence, (4) provides a picture of how the velocity loop operates, as highlighted by the following comments:

- T_f contains a contribution of the type $-(J_f s^2 + C_f s + K_f s)$ to the left–hand side of (4), which affects the high–frequency response by decreasing the inertia, damping, and elastic forces. In fact, in the ideal case of exact knowledge of their true values, they would be cancelled, thus expediting the transient tracking response.

  Even if it is anticipated that it will not be used in this work, a feed–forward with J_f, C_f, and K_f determined according to a quasi–steady aerodynamic approximation of a control surface hinge moment, could provide an effective adaptation against changing flight conditions, without affecting system stability. From this perspective, it is worth remarking that this feed–forward could be a simpler and effective substitute for the previously mentioned possible addition of J_f, C_f, and K_f to J, C, and K.

- The transfer function ω/ω_r has no zeros; therefore, through an appropriate design, the actual velocity tracking overshoots should be close to zero or maintained as small as possible.

- The integral terms can cancel time–varying piecewise polynomial disturbances, whose frequency contents are within the velocity bandwidth up to time order t^{m-1}.

- With corresponding reasoning, it can be seen that the low frequency part of the velocity transfer function up to s^{m-2} does not depend on the system parameters for non–null C and K. Independence increases to s^m if they are null. Thus, the higher the value of m the lower the low–frequency sensitivity of the closed loop response to J, C, K uncertainties. In particular, $m = 2$ is required to achieve steady–state velocity in the face of piecewise constant disturbances. Nonetheless, because of the Bode Integral theorem [32], the higher the desensitization, the higher the sensitivity to out–of–band disturbance. This fact poses a constraint on the corresponding achievable bandwidth for growing m [33], [34].

B. POSITION LOOP

The substitution of (2c) into (4) leads to:

$$\left(Js^{m+1} + (C + k_P^v)s^m + (K + k_{I,1}^v)s^{m-1} + \sum_{i=2}^{m} k_{I,i}^v s^{m-i} \right)s^n\omega + k_{I,m}^v \cdot \left(\sum_{j=0}^{n} k_{I,j}^p \right)\theta$$
$$= \left(k_{I,m}^v \omega_f + T_f s^m \right)s^n + k_{I,m}^v k_{I,n}^p \theta_r + T_d s^{m+n} \tag{5}$$

so that, being $s^n\omega = s^{n+1}\theta$, one has:

$$
\left[Js^{n+m+2} + (C + k_P^v)s^{n+m+1} + (K + k_{I,1}^v)s^{n+m} \right.
$$

$$
\left. + \sum_{i=2}^{m} k_{I,i}^v s^{n+m+1-i} + k_{I,m}^v \cdot \left(\sum_{j=0}^{n} k_{I,j}^p s^{n-j} \right) \right] \theta
$$

$$
= k_{I,m}^v \left(k_{I,n}^p \theta_r + \omega_f s^n \right) + T_d s^{n+m} + T_f s^{n+m} \tag{6}
$$

representing the operational form of the controlled system response, which is driven only by the reference rotation command θ_r multiplied by the two highest order integral gains $k_{I,m}^v$ and $k_{I,n}^p$.

It is therefore possible to remark that:

- For $\omega_f = 0$, owing to the already mentioned feature of commanding just through the highest order integral, or proportional terms at most, no derivative of ω_c and θ_r appears; that is, there is no controller zero in the closed loop transfer function. This is an important property of a nominal design model based on the assignment of a prototype closed loop transfer function.
- If some derivatives of the reference commands are deemed useful, for example, to expedite the closed loop response, they can be applied using ω_f and/or the torque feed–forward scheme of the velocity loop. The related gains and derivative calculations can be optimized for the required performances in a fully independent manner from the implementation of the prototyped closed loop transfer function.
- The higher the order of the integral terms, the more independent the system parameters will be in the low–frequency response. Therefore, the last comment associated with the velocity loop can be applied to the n integrations position loop.
- At the rotation level, the order of the time–varying piecewise polynomial disturbances that can be cancelled is increased by n.

C. DESIGN EQUATIONS

Because the two loops are driven simply by applying the position/velocity errors to the highest order integral, after omitting the feed–forward and disturbance terms, the nominal closed loop transfer function, $H_c(s)$, associated with a 3 dB attenuation at the low–pass bandwidth ω_0 and without any zero, can be derived from (6) and written as:

$$
H_c(s) = \frac{\theta}{\theta_r} = \frac{N_c}{D_c(s)} \tag{7}
$$

where $N_c = k_{I,m}^v k_{I,n}^p \theta_r$ and $D_c(s)$ is the left–hand side in square brackets of (6). Consequently, $D_c(s)$ and N_c can be abstracted as $D_c(s) = \sum_{j=0}^{m+n+2} a_j (\omega_0/s_f)^j s^{m+n+2-j}$ and $N_c = a_{m+n+2}\omega_0^{m+n+2}$, where a_is are the coefficients of a chosen prototype transfer function, normalized for $\omega_0 = 1$, s_f is a possible scale factor required to satisfy the 3 dB constraint at $\omega_0 = 1$. Therefore, the design of the controller can be based on assigning its $(n + m + 2)$ gains to match

the desired transfer function prototype with no commanded position overshoots. Such a choice aims to avoid bumps against end of run hard points and should further be coupled to negligible violations of any possible velocity constraint, related either to the current drive or to the need to emulate an actuator of different kinds. Assuming precise knowledge of the parameters in (1), two denominator prototypes apt to satisfy the previously cited design features are binomial power and Bessel–Thomson filters. Owing to its somewhat better gain and phase margins, the former is the preferred choice. Regardless the chosen pole prototype, the related assignment solution is based on matching each coefficient of $D_c(s)$ with its corresponding left–hand term in (6), leading to the following trivial gain calculations:

$$
\text{velocity loop} \quad
\begin{cases}
k_P^v = a_1 \cdot \omega_0 \cdot J - C \\
k_{I,1}^v = a_2 \cdot \omega_0^2 \cdot J - K \\
\quad\vdots \\
k_{I,i}^v = a_{i+1} \cdot \omega_0^{i+1} \cdot J \\
\quad\vdots \\
k_{I,m}^v = a_{m+1} \cdot \omega_0^{m+1} \cdot J
\end{cases} \tag{8a}
$$

with the constraint $m \geq 1$, so to reduce the sensitivity imprecisely known C and K and:

$$
\text{position loop} \quad
\begin{cases}
k_P^p = a_{m+2} \cdot \omega_0^{m+2} \cdot J/k_{I,m}^v \\
k_{I,1}^p = a_{m+3} \cdot \omega_0^{m+3} \cdot J/k_{I,m}^v \\
\quad\vdots \\
k_{I,i}^p = a_{m+i+2} \cdot \omega_0^{m+i+2} \cdot J/k_{I,m}^v \\
\quad\vdots \\
k_{I,n}^p = a_{m+n+2} \cdot \omega_0^{m+n+2} \cdot J/k_{I,m}^v
\end{cases} \tag{8b}
$$

The above list of gain formulae clearly confirms what was previously stated, that is, that all the control gains, except k_P^v and $k_{I,1}^v$, do not depend on the design parameters C, K, making the formulation somewhat insensitive to possible model uncertainties. This feature, combined with the capability of compensating piecewise bounded polynomial disturbances of a relatively high order, might make it unnecessary to schedule servo gains against significant unmodeled external loads owing to the changing aerodynamic forces applied to the control surfaces.

As previously stated, a simple binomial polynomial structure nominally satisfying the aforementioned design goal is of the type $(s + \omega_0/s_f)^{m+n+2} = 0$, with the range of the s_f scaling factors of interest for this study given in Table 1.

TABLE 1. Pass band scaling for $(s + \frac{\omega_0}{s_f})^k$.

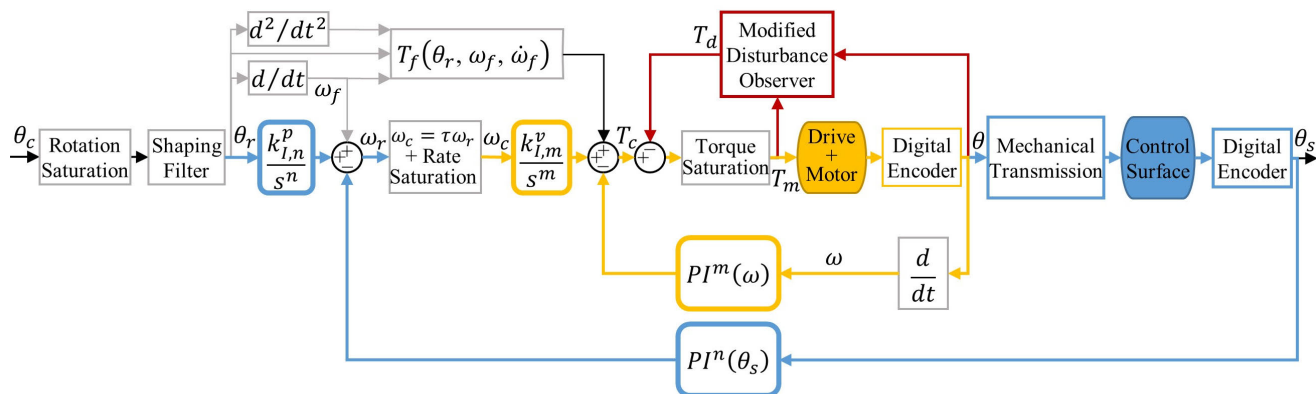| k	3	4	5	6	7
s_f	0.50885	0.43417	0.38491	0.34931	0.32205

FIGURE 2. Implemented dual loop controller scheme.

D. DUAL SENSOR IMPLEMENTATION AND ANTI–WINDUP COMPENSATION

Although an almost rigid connection between the motor and the control surface was assumed for the design of the controller described in the previous section, the actual implementation was based on two independent sensors, as shown in Fig. 2. Torque saturation and high sliding friction apart, owing to the adoption of a harmonic motor drive with no free–play and well defined parameters, such a choice allows the implementation of a velocity loop that is linear, with negligible uncertainties and fairly close to its design assumptions. Moreover, it comes with an encoder with three times the resolution of the one attached to the ailerons, thus providing better values for deriving the motor velocity. In such a view, (2) is recast in the following input–output equations:

$$s^n \omega_r = k_{I,n}^p \cdot (\theta_r - \theta_s) - \sum_{j=0}^{n-1} k_{I,j}^p s^{n-j} \theta_s + s^n \omega_f \quad (9a)$$

$$\omega_c = \tau \, \omega_r \quad (9b)$$

$$s^m T_c = k_{I,m}^v \cdot (\omega_c - \omega) - \sum_{i=0}^{m-1} k_{I,i}^v s^{m-i} \omega + s^m T_f \quad (9c)$$

where θ_s is the control surface rotation, and it is evident that the errors $(\theta_r - \theta_s)$ and $(\omega_c - \omega)$ are applied only to the highest order integral or, when no integration is used, to the proportional term.

Then, for m and $n > 0$, they can be unified in the following scheme:

$$\begin{cases} sx_{I,1} = x_{I,2} - k_{I,1}y \\ sx_{I,2} = x_{I,3} - k_{I,2}y \\ \quad \vdots \\ sx_{I,l-1} = x_{I,l} - k_{I,l-1}y \\ sx_{I,l} = k_{I,l} \cdot (y_c - y) \end{cases} \quad (10)$$

$$u = x_{I,1} - k_{I,0}y + u_f \quad (11)$$

with:

- $k_{I,...} = k_{I,...}^v \mid k_{I,...}^p, \, l = m \mid n$;
- $y = \theta_s \mid \omega$;

- $y_c = \theta_r \mid \omega_c$;
- $u_f = \omega_f \mid T_f$;
- $u = \omega_c \mid T_c$

calling | the logical "or", which allows the same formulation to be used for both the position and velocity loop.

The above equations readily lead to the following state–space representation of the PI^{m}PI^n controllers:

$$\begin{Bmatrix} \dot{x}_{I,1} \\ \dot{x}_{I,2} \\ \vdots \\ \dot{x}_{I,l-1} \\ \dot{x}_{I,l} \end{Bmatrix} = \begin{bmatrix} 0 & 1 & 0 & 0 & 0 \\ 0 & 0 & 1 & 0 & 0 \\ \vdots & \vdots & \ddots & \vdots & \vdots \\ 0 & 0 & 0 & 0 & 1 \\ 0 & 0 & 0 & 0 & 0 \end{bmatrix} \begin{Bmatrix} x_{I,1} \\ x_{I,2} \\ \vdots \\ x_{I,l-1} \\ x_{I,l} \end{Bmatrix}$$
$$+ \begin{bmatrix} -k_{I,1} & 0 & 0 \\ -k_{I,2} & 0 & 0 \\ \vdots & \vdots & \vdots \\ -k_{I,l-1} & 0 & 0 \\ -k_{I,l} & k_{I,l} & 0 \end{bmatrix} \begin{Bmatrix} y \\ y_c \\ u_f \end{Bmatrix} \quad (12)$$

$$u = \begin{bmatrix} 1 & 0 & 0 & . & . & . & 0 \end{bmatrix} \begin{Bmatrix} x_{I,1} \\ x_{I,2} \\ \vdots \\ x_{I,l-1} \\ x_{I,l} \end{Bmatrix}$$
$$+ \begin{bmatrix} -k_{I,0} & 0 & 1 \end{bmatrix} \begin{Bmatrix} y \\ y_c \\ u_f \end{Bmatrix} \quad (13)$$

Defining $\mathbf{x}_l = \{x_{I,1} \, x_{I,2} \, \ldots \, x_{I,l-1} \, x_{I,l}\}^T$ and $\mathbf{y} = \{y \, y_c \, u_f\}^T$, the above equation can be synthesized as a standard linear time–invariant system in the form

$$\dot{\mathbf{x}}_I = \mathbf{A}\mathbf{x}_I + \mathbf{B}\mathbf{y}$$
$$u = \mathbf{C}\mathbf{x}_I + \mathbf{D}\mathbf{y} \quad (14)$$

and the observer–like anti–windup formulation of [35] and [36] can be easily adapted to (14), that is, from [35]

$$\dot{\mathbf{x}}_I = \mathbf{A}_I \mathbf{x}_I + \mathbf{B}_I \mathbf{y} + \mathbf{L} u$$
$$v = \mathbf{C}\mathbf{x}_I + \mathbf{D}\mathbf{y}$$
$$u = sat(v) \quad (15)$$

with:

$$sat(v) = \begin{cases} V_{low} & v \le V_{low} \\ v & V_{low} < v < V_{high} \\ V_{high} & v \ge V_{high} \end{cases} \quad (16)$$

$V_{low}|V_{high}$ being either $\Omega_{c,low} = \tau\,\Omega_{s,low}|\Omega_{c,high} = \tau\,\Omega_{s,high}$ or $T_{c,low} \mid T_{c,high}$, with $\mathbf{A}_I = \mathbf{A} - \mathbf{LC}$, $\mathbf{B}_I = \mathbf{B} - \mathbf{LD}$ and $\mathbf{L}$ an appropriate observer gain matrix that will be designed trough a pole placement scheme. According to the notation of the generic value v, $\Omega_{s,low}$ and $\Omega_{s,high}$ are the highest and lowest values of velocity ω_s. It is further trivially remarked that $\theta_r = sat(\theta_c)$, with $V_{low} = \Theta_{s,low}$ and $V_{high} = \Theta_{s,high}$, being $\Theta_{s,low}$ and $\Theta_{s,high}$ the allowed highest and lowest values of the rotation θ_s.

Hence, if $\mathbf{A}_I$ is in a cascaded integrator form, the matrix $\mathbf{L}$ will simply be

$$\mathbf{L} = \begin{bmatrix} a_1\omega_0 & a_2\omega_0^2 & \ldots & a_i\omega_0^i & \ldots & a_l\omega_0^l \end{bmatrix}^T \quad (17)$$

where ω_0 is the desired low–pass band of the resulting anti–windup observer, and the a_is are the coefficients of the prototype design polynomials $P_i(s) = \sum_0^n a_i\omega_0^i s^{n-i}$, of the low–pass Butterworth type in this work, normalized for $\omega_0 = 1$. The definition used for P_i refers to easily found normalized Butterworth polynomials [37], for which $s_f = 1$.

In relation to the more modern integrated designs of controllers embedding an anti–windup scheme [38], the approach adopted here was chosen because of its simple design and adequate performance.

When m or n is null, the trivial control to be applied is simply

$$u = sat(k_{I,0}(y_c - y) + u_f) \quad (18)$$

without any windup action to be cared of.

E. DISTURBANCE OBSERVER

Disturbance observers [39] can be used as a substitute for integral control [40] and are the basis for the disturbance accomodating controls (DAC) proposed by [41] and [42], as well as an essential component of active Disturbance Rejection Controls (ADRC) found in [43] and [44].

Following [41] and [42], we adopt the DAC–like scheme depicted in Fig. 2. Nonetheless, the way it is used will lead to a specialized kind of disturbance rejection. In fact, for relatively slow piecewise polynomial disturbances, that is, varying within the PI^{m}PI^n bandwidth, the type of DAC observer to be used would end in monitoring the same disturbances already identified and suppressed by the integral terms of our controller, thus ending in being of little use. Therefore, the observer will be designed to do something more and differently, that is, to suppress the relatively higher frequency content of the observed disturbances, that is, the out–of–band disturbances that are not suppressed by the integral terms. Observers for bounded piecewise polynomial disturbances of order up to t^2 can be expressed in the

following state space representation:

$$\begin{Bmatrix} \dot\theta \\ \ddot\theta \\ \dot T_d \\ \ddot T_d \\ \dddot T_d \end{Bmatrix} = \begin{bmatrix} 0 & 1 & 0 & 0 & 0 \\ -K/J & -C/J & 1/J & 0 & 0 \\ 0 & 0 & 0 & 1 & 0 \\ 0 & 0 & 0 & 0 & 1 \\ 0 & 0 & 0 & 0 & 0 \end{bmatrix} \begin{Bmatrix} \theta \\ \dot\theta \\ T_d \\ \dot T_d \\ \ddot T_d \end{Bmatrix}$$
$$+ \begin{bmatrix} 0 \\ 1/J \\ 0 \\ 0 \\ 0 \end{bmatrix} T_m \quad (19)$$

$$y = \begin{bmatrix} 1 & 0 & 0 & 0 & 0 \end{bmatrix} \begin{Bmatrix} \theta \\ \dot\theta \\ T_d \\ \dot T_d \\ \ddot T_d \end{Bmatrix} \quad (20)$$

Therefore, defining $\mathbf{x}_f = \{\theta\; \dot\theta\; T_d\; \dot T_d\; \ddot T_d\}^T$, the observer can be defined through:

$$\dot{\mathbf{x}}_f = \mathbf{A}_f \mathbf{x}_f + \mathbf{B}_f \cdot T_m + \mathbf{L} \cdot y$$
$$y = \mathbf{C}\mathbf{x}_f \quad (21)$$

where $\mathbf{A}_f = \mathbf{A} - \mathbf{LC}$, $\mathbf{B}_f = \mathbf{B}$ and $\mathbf{L}$ is the observer gain matrix, once more designed through a pole placement scheme based on Butterworth filter prototypes, denoted as $P_o(s) = \sum_0^n a_i\omega_0^i s^{n-i}$, so that $\mathbf{L}$ is given by

$$\begin{cases} L_1 = ((a_1 \cdot \omega_0 \cdot J - C)/J \\ L_2 = \left(a_2 \cdot \omega_0^2 \cdot J - C \cdot L_1 - K\right)/J \\ L_3 = a_3 \cdot \omega_0^3 \cdot J \\ L_4 = a_4 \cdot \omega_0^4 \cdot J \\ L_5 = a_5 \cdot \omega_0^5 \cdot J \end{cases} \quad (22)$$

The above equation can be used for T_d and any order of its derivatives, including the extension of the observer order to $\frac{d^k T_d}{dt^k}$ with $k > 2$, for which $L_{k+3} = a_{k+3}\,\omega_0^{k+3}\,J$.

Nonetheless, as discussed in Section II and previously pointed out again, it should be noted that the PI^{m}PI^n controller disturbance compensation is limited by its bandwidth, whereas the disturbance observer can be designed with a higher bandwidth. Even so, its compensating contribution proved negligible, while a minor observer–based feedback loop, described in the next section, has been effective against the mentioned out–of–band disturbances.

F. DIGITAL CONVERSION

Saturation apart, which remains as in (16) at each controller sampling, (15) and (21) have the same observer–like structure, here unified as:

$$\dot{\mathbf{x}}_o = \mathbf{A}_o\mathbf{x}_o + \mathbf{B}_o\mathbf{u}_o + \mathbf{L}y_o$$
$$y_o = \mathbf{C}\mathbf{x}_o + \mathbf{D}\mathbf{u}_o \quad (23)$$

To digitally implement the above unifying continuous time form, (23) is discretized using the standard zero–order hold

state transformation, leading to the following prediction form [40]:

$$\mathbf{x}_o(k+1) = \mathbf{\Phi}\mathbf{x}_o(k) + \mathbf{\Gamma}_B\mathbf{u}_o(k) + \mathbf{\Gamma}_L\mathbf{y}_o(k)$$
$$y_o(k) = \mathbf{C}\mathbf{x}_o(k) + \mathbf{D}\mathbf{u}_o(k) \tag{24}$$

with $\mathbf{\Phi} = e^{\mathbf{A}_o\Delta t}$, $\mathbf{\Gamma}_B = \int_0^{\Delta t} e^{\mathbf{A}_o\tau}\mathbf{B}_o\,d\tau$ and $\mathbf{\Gamma}_L = \int_0^{\Delta t} e^{\mathbf{A}_o\tau}\mathbf{L}\,d\tau$, where Δt is the sampling time and k is used to define the k–th time step. The choice of the sampling time Δt depends on both the sampling frequency ($\Delta t = 1/f_s$), which requires satisfying the needs listed later in this section, and the specific controller design, as will be discussed in subsection III-C for the test case considered in this work.

Then, using any standard and, especially for relatively high m and n, a well–conditioned pole assignment method [45], it is possible to design $\mathbf{\Gamma}_L$ using either (23) or (24). Given the simple closed form solutions already available for the continuous form, anticipating the adoption of an adequate sampling rate, the former approach was chosen.

The previously hinted idea of a special form for accounting for external disturbances beyond the capability already embedded in a PI^{m}PI^n controller, is based on the conjecture that this disturbance compensation could be made more effective by correcting the control torque T_c with the resulting torque $T_d + T_c$. Therefore, instead of the usual setting $T_m = T_c$, the following discrete form is used:

$$T_m(k) = T_c(k) - \mu(T_d(k) + T_m(k-1)) \tag{25}$$

where $T_d(k)$ is the disturbance predicted from $T_m(k-1)$ and $\theta(k-1)$ at the end of the $k-1$ step and μ is a possible tuning parameter, which is maintained as $\mu = 1$. Thus, the observer can provide additional feedback on the motor torque command, which improves the suppression of high frequency disturbances. The complete scheme of the modified disturbance observer, including both observers (21) and the additional feedback, is shown in Fig. 3. A justification for this conjecture is given shortly, based on a sample of measured data.

The criteria for an adequate choice of the discretizing sampling frequency f_s should consider the following:

- avoid causing unacceptable delays to active controllers commanding the control surfaces without unduly constraining their own sampling time and/or any synchronization with the surface servo sampling;
- adequately discretizes the PI^m velocity loop, which has bandwidth approximately three times higher than that of the position loop;
- provide an adequate discretization of the disturbance observer so that it is possible to estimate disturbances at frequencies higher than the bandwidths of the position and velocity loops;
- mitigate the aliasing associated with the position encoders, the unknown delay related to the current drive, and the delay ($\Delta t/2$) of the–zero order hold controller output;
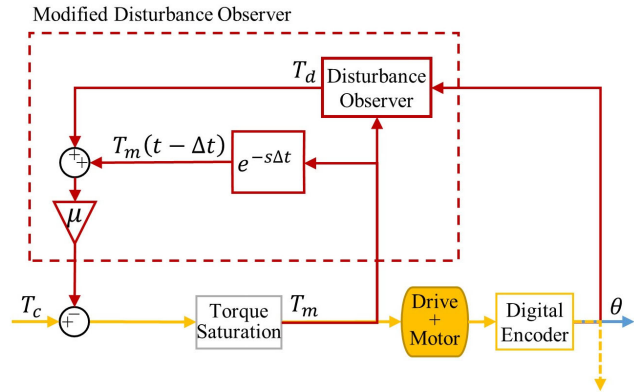

FIGURE 3. Modified disturbance observer scheme.

- for better numerical conditioning, (24) implements discretized continuous designs using the so called δ–Operator approach [36], [46].

The above needs can be satisfied with a sufficiently high sampling frequency, which is assumed to be on the order of 50 times the velocity bandwidth. It is noted that we will eventually incur constraints, similar to those mentioned above, when our torque command, T_c, is passed to the Digital Signal Processing in charge of the current drive, likely running in the range of a few kHz.

It is worth noting that the velocity used for the internal loop is not the one provided by the disturbance observer but is instead obtained after acquiring the input of the two encoders, at the very beginning of each sampling instant. The problem of adequately deriving both fast and slow velocities associated with encoder position measurements has a large body of literature. An interesting instance was presented in [47], whereas a commonly used industrial approach can be found in the reference manual [48]. Our solution is based only on the latter approach, which is simply based on keeping a record of the most recently measured positions, from which one can compute the velocity using: $\omega(k) = (\theta(k) - \theta(k-d))/(t(k) - t(k-d))$, where d is the closest to k backward time offset of the previously measured values for which $(\theta(k) - \theta(k-d)) \geq \Delta\Theta$, $\Delta\Theta$ being assigned on the basis of the encoder resolution. A possible analysis of the error incurred using this approach, with a criterion for assigning d in relation to a given $\Delta\Theta$, is proposed by [49]. Although trivial, it must be noted that this approach embeds a moving average low–pass filter whose length is inversely proportional to the velocity, thus providing a natural adaptive filter delay without causing instabilities.

III. CONTROLLER DESIGN

The controller described in the previous section was applied to the inner aileron of the GLAMOUR wind tunnel demonstrator [30]. This aileron is shown in Fig. 4, where it is possible to see how a belt drive allows housing the actuation system inside the wing trailing edge thickness of the inner and outer ailerons, the former being used here as the test
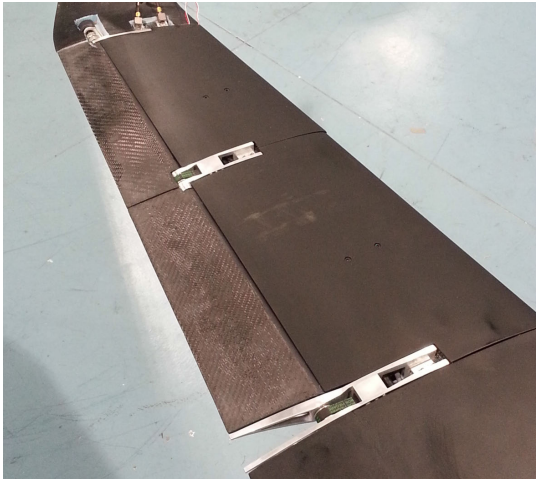
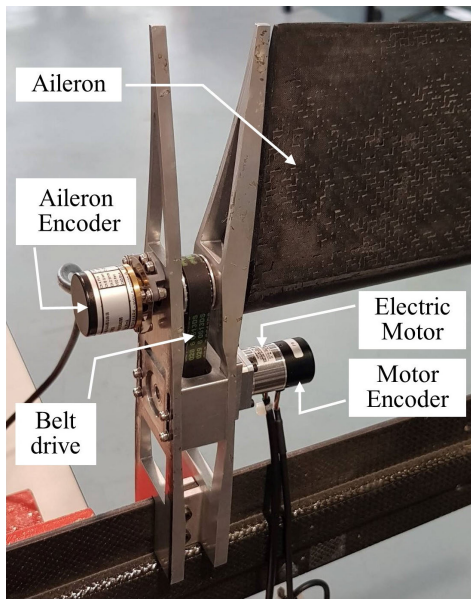**FIGURE 4.** Double aileron wing configuration of the wind tunnel demonstrator.

FIGURE 5. Dual encoder servo actuation system installed on the aileron test bench.

bench. The two–sensor actuation system installed on the test bench is shown in Fig. 5, where the aileron is indirectly driven by a *Harmonic Drive®️ RSF–5B* supermini brushless motor coupled to a harmonic speed reducer.

Harmonic Drive®️ was selected because of the high performance of its gearing technology, which guarantees zero backlash and high torque in a compact device. A large pulley diameter was selected to perfectly fit the external wing shape, whereas the belt width and length were chosen to not exceed the maximum allowable tension. Once these design parameters are established, the motor gear ratio and small pulley diameter are defined to achieve the torque requirement, considering an appropriate safety margin. The design requirements in terms of maximum torque and bandwidth were computed by several aeroservoelastic simulations that went through as many design phases as the wind tunnel model [26].

The motor, transmission, and aileron data of interest are as follows:

- maximum torque at the output shaft: $T_M = 0.9\,\text{N m}$, to be used as torque saturation value;
- harmonic speed reduction: 50;
- expected stiction at the output shaft of 0.288 N m (from the motor manual [50]);
- nonlinear transmission stiffness at the output shaft ranging from 110 N m to 170 N m, with an angular hysteresis of up to 0.1 deg;
- belt drive transmission ratio: $\tau = \theta/\theta_s = 22/14$;
- allowed maximum output shaft angular speed: $540\,\text{deg s}^{-1}$;
- allowed maximum radial load on the output shaft: 90 N;
- motor encoder: 500 pulses per revolution, multiplied by 4 through quad sampling, resolution at the output shaft: 0.0036 deg;
- *Scancon 2RMHF* aileron encoder: 7500 pulses per revolution, multiplied by 4 through quad sampling, resolution: 0.012 deg;
- allowed maximum aileron angular speed of $350\,\text{deg s}^{-1}$, that is, the actual saturation to be imposed at the output motor shaft is $550\,\text{deg s}^{-1}$;
- estimated maximum control surface hing moment: $T_s = 1.4\,\text{N m}$, matching the maximum torque at the motor output shaft.

A. PI^m PI^n BASE DESIGN

Continuous–time designs were carried out using the analytical approach described in subsection II-C. The selected prototype transfer function is:

$$(s + \omega_0/s_f)^{m+n+2} = 0$$

with $\omega_0 = f_0/2\pi$. The wind tunnel demonstrator described above was designed based on an iso–frequency scaling strategy; that is, the frequencies of the most relevant vibration modes of the demonstrator were equal to those of the full–scale GRA. This scaling also dictated the servo actuator bandwidth which was required to be $f_0 = 10$ Hz. The controller gains are computed using (8), where the motor inertia is obtained from the motor manual, and the control surface inertia is calculated using its CAD model. The designs are based only on the data shown in Table 2, that is, with C and K set to zero. This allows a first–hand assessment of the insensitivity of the chosen pole assignment to uncertain design parameters on the basis of both the usual Phase and Gain Margins (PM and GM) and the bounds derived from their conservative peak counterparts (pPM and pGM), as obtained from the sensitivity and complementary sensitivity functions [51], [52].

TABLE 2. Aileron and belt drive data.

J_m (kg m²)	J_a (kg m²)	τ	J (kg m²)
$1.83 \cdot 10^{-4}$	$7.9 \cdot 10^{-5}$	22/14	$2.153 \cdot 10^{-4}$

TABLE 3. Phase and Gain Margins for the position loop (upper value) and the velocity loop design (lower value), as a function of *m*.

m	f_0 (Hz)	PM (deg)	GM (dB)	pPM $\geq$ (deg)	pGM (dB)
1	10.0	71.2	9.10 (19.1)	60.0	$GM_{max} \geq 4.50$ (13.1)
	26.7	72.4	*Inf*	60.0	$GM_{min} \leq 0.16$ (-15.7)
3	10.0	66.9	3.89 (11.9)	60.0	$GM_{max} \geq 3.21$ (10.1)
	28.4	66.9	0.27 (-11.4)	60.1	$GM_{min} \leq 0.32$ (-9.9)
4	10.0	65.8	3.37 (10.6)	60.0	$GM_{max} \geq 2.96$ (9.4)
	29.5	65.8	0.30 (-10.5)	60.1	$GM_{min} \leq 0.34$ (-9.4)
5	10.0	65.0	3.08 (9.8)	60.0	$GM_{max} \geq 2.80$ (8.9)
	30.1	65.0	0.32 (-9.9)	60.1	$GM_{min} \leq 0.36$ (-8.9)

Several designs were evaluated, simulated, and tested, but it is impractical to analyze all possible m/n combinations. Thus, Table 3 displays only the results of the design eventually chosen for the wind tunnel tests, that is, with $n = 0$ for a simple proportional position feedback and $m = 3 : 5$ for the PI velocity loops. In this table, for each m, the upper row refers to the rotation loop, the lower row refers to the velocity loop, f_0 is the corresponding -3 dB bandwidth. The reason for such a final design choice is that for the same $m + n$ order of the closed loop position transfer function, allowing the velocity loop to have the maximum possible order provides the best results in the validation test results. In fact, from the introduction, it is possible to verify that a simple PID, that is, $u = -(k_d s^2 + k_p s + k_{i1})/s \cdot y$, can be implemented in a dual loop form by setting: $k_P^v = k_d$, $k_{I,1}^v = k_p$ and $k_P^p = k_{i1}/k_p$. From Table 3, it can be seen that from the point of view of linear margins, a simpler PID seems to be better than the schemes aimed at replacing it. Nonetheless, even if the margins of Table 3 still provide a valuable indication of the insensitivity to uncertain design parameters, for thorough validation, there remains a need for stricter validation against nonlinear issues. These aspects will be verified further using a more accurate numerical model, followed by an extensive set of experimental tests.

B. DISTURBANCE OBSERVER AND ANTI–WINDUP COMPENSATOR DESIGN

Similar to the controller design, the disturbance observer was designed through pole assignment in continuous time and then discretized. The chosen Butterworth pole prototype bandwidth was equal to the passband of the associated $PI^m PI^n$ controller velocity loop.

Through a series of simulations, it was verified that the bandwidth of the third order observer described in subsection II-E adequately estimated the modeled friction and random disturbances as piecewise varying constants. Therefore, regardless of the coupled $PI^m PI^n$ controller, only this structured disturbance observer was used in the numerical and experimental tests, which will be discussed later in this paper.

The anti–windup compensators were designed along the same lines, with a bandwidth equal to that of its loop.

C. SAMPLING FREQUENCY

Because of the aforementioned iso–frequency scaling and the need to emulate a full–scale EMA solution for the actuating systems, during the various phases of the GLAMOUR project [30] and one of its extensions [53], the bandwidth of the actuators has always been maintained at 10 Hz. On the other hand, in order to follow the sampling rate guide lines listed in subsection II-F, the actual rate values for the actuators had to vary in relation to the sampling frequencies of the diverse gust controllers under test, as dictated by their designers. Because one of the last and most demanding active gust controllers required a 400 Hz rate with an acceptable delay of no more than one–third of its period, the actuator sampling rate was set at 1500 Hz. Therefore, because it satisfies the mentioned guide lines, it remains the sampling rate used for what was reported in the following.

IV. EXPERIMENTAL TEST RIG SETUP

The experimental setup, in terms of hardware and real–time environment, consists of a system developed at the Department of Aerospace Science and Technology, Politecnico di Milano, to provide standardized support for managing wind tunnel models of active aeroelastic control systems. It was designed to be a modular, small, and weight system to be installed on board different models. It is capable of completely managing control tasks and Input/Output (I/O) signals. It consists of three separate parts, the first two being shown in Fig. 6:

- a PC-104 equipped with: a 4 core INTEL-ATOM-E3845 1.9 GHz; PCI boards for managing: 32-16bits analog input, 4-16bits analog output, 8-24bits encoders, 24 TTL digital I/O, 16-24V industrial digital I/O, used to supervise the motor drives;
- a drive box for up to three *Harmonic Drive*®1G motors;

An out–of–board power box supplies all that is onboard. The support for all digital control systems is provided by a Real–Time Application Interface (RTAI), a hard–real–time extension for Linux, developed in–house. RTAI is in charge of both the actuator controllers described here, coded in C, and the active gust/flutter controllers, generated by MATLAB Simulink–RTW (Real Time Workshop) toolboxes. The entire system is then remotely and interactively supervised through an RTAI extension called QRTAILab [54].
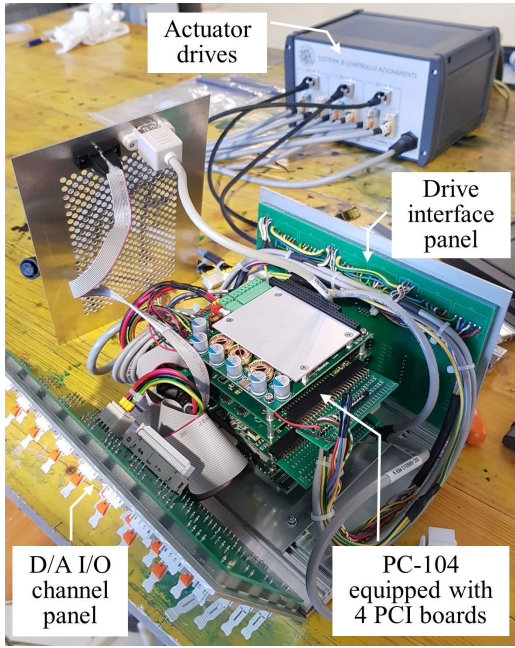
FIGURE 6. Modular system consisting of the PC–104 embedding I/O system (bottom of the picture) connected to the motor drives (top of the picture).

The working test rig was obtained by connecting the modular system to the aileron test bench, as shown in Fig. 5. The setup was then completed by applying tension to the belt. Somewhat troubling condition because of the constraint imposed by the maximum allowable radial load applicable to the motor shaft is exceeded by simply applying a symmetric tension corresponding to the force that generates only half of the maximum allowed motor torque. For a reasonable long–term service, the inevitable compromise is to apply a pretension of approximately one–third of the admissible radial load. This condition was roughly verified by measuring the deflection at the middle span owing to the applied transverse load. This is a common yet imprecise method suggested for many timing belt manuals. Assuming a negligible belt bending stiffness, the trivial string–like relation required for the approximated verification of a proper tensioning is $P = 4(T/L)f$, where P is the required mid–span transverse load, T is the per span tension, L is the per span belt length, and f is the middle span transverse displacement. After roughly achieving the established tension setup, the transmission was verified against possible residual free–play. For this purpose the aileron was repeatedly driven to softly hit the aileron end of the run stops by commanding motor torque in the open loop. Subsequently, a reversed torque value was applied, and the measures of the motor and aileron encoder were registered. The processing of the acquired data provided a free–play of 0.5 ± 0.1 deg. The feasibility of dynamically working with this combination of pretension and free–play was eventually verified by applying open loop sinusoidal motor torques up to half of the maximum torque at 7 Hz.

Eventually, using the same procedure, a lower pretension associated with a measured free–play of approximately 1.5 deg was verified to produce no belt ratcheting (tooth jumping) under smoothly driven motor torques.

Repraising a short remark of the introduction, it is worth recalling that the PID used before the adoption of the design approach presented in this paper, that is, [26] and [27], did not care for the mentioned radial load constraint and applied a substantially backlash free higher tensioning, which led to the loss of one motor while damaging a still usable another one.

V. NUMERICAL AND EXPERIMENTAL TEST RESULTS

Numerical simulations were only loosely addressed in the previous sections of this paper. The related model used during the validation phase, described here, considers linear and nonlinear aspects that have been intentionally neglected in the controller design, as anticipated at the end of subsection III-A. Because some significant simulated results are now going to be presented, there is clearly the need to show what is behind them, that is,

$$\dot{T}_i = -\omega_i \cdot T_i + \omega_i \cdot T_m \tag{26a}$$

$$J_s \ddot{\theta}_s = N_b \cdot r_s - C_b(\dot{\theta}_s \cdot r_s - \dot{\theta} \cdot r_m)$$
$$+ T_{ae} - K_{ae}\theta_s - C_{ae}\dot{\theta}_s + T_{sf} + T_{rs} \tag{26b}$$

$$J_m \ddot{\theta} = -N_b \cdot r_m - C_b(\dot{\theta} \cdot r_m - \dot{\theta}_s \cdot r_s)$$
$$+ D \cdot T_i + T_{mf} + T_{rm} \tag{26c}$$

$$N_b = N_b(K_b, \theta_{fp}, \theta_s \cdot r_s, \theta \cdot r_m) \tag{26d}$$

where T_i and ω_i are the output torque and bandwidth of the current drive, $J_s = J_a + J_{ae}$ is the total aileron moment of inertia, which is the sum of J_a and J_{ae} the incompressible aerodynamic mass moment, N_b is the nonlinear belt tension, K_b is the belt stiffness, θ_{fp} is the free–play at the aileron pulley, r_s and r_m are the radii of the aileron and motor pulleys, C_b is the viscous belt damping, T_{sf} and T_{mf} are the Coulomb friction at the aileron and motor, T_{ae} is the trim hinge moment to which the commanded position is superimposed, K_{ae} and C_{ae} are the quasi–steady approximations of the aero-dynamic hinge moment stiffness and damping, respectively, T_{rs} and T_{rm} are the random torque disturbances applied to the aileron and motor, D is a multiplicative factor taking into account a possible imprecise scaling of the commands to the motor drive. Even if these equations are still a type of medium–fidelity model, they highlight the most significant terms affecting the performance of the system at hand.

To account for the nonlinearities associated with free–play and sliding friction, model (26) is integrated using explicit second order Runge–Kutta methods, chosen among the Runge–Kutta–Heun, Runge–Kutta–Heun–Ralston, and mid–point approximations. Their integration can be carried out either in true or to expedite simulations and false real time. If required, numerical stability and improved precision could be achieved by sub–stepping within each control sample.
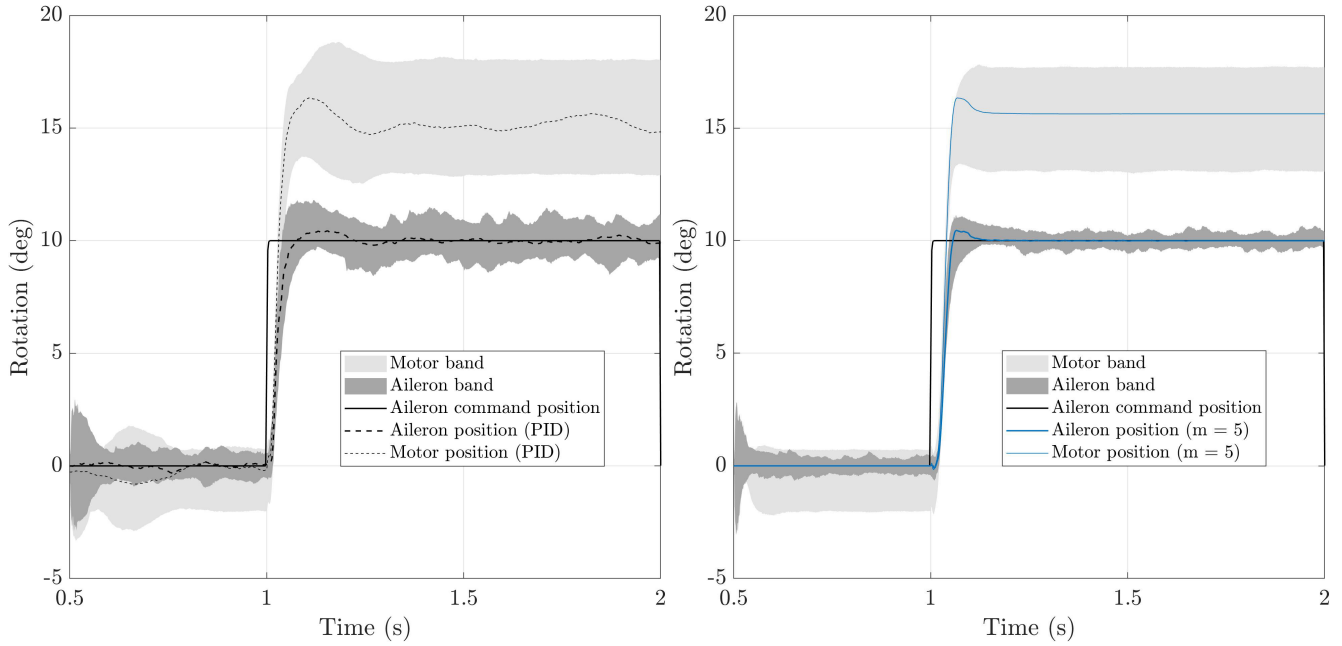
FIGURE 7. Uncertainty propagation of a step response for the PID controller (left) compared with the PI^{5}PI^0 controller (right).

A. MONTE CARLO EVALUATION OF DESIGN UNCERTAINTIES

The standard PM and GM shown in subsection III-A, supported by their mated conservative pPM and pGM bounds, could already be an indication of robustness. Nonetheless, they are associated with a very sketchy model, discarding many significant terms modeled in (26). However, keeping as a firm point out the need for a simple design method to be trusted at the face of basing it on just a very few and reasonably known parameters, there remains a need for a more thorough validation against the uncertainties associated with the above equations. For this purpose, the chosen approach was a fairly detailed Monte Carlo simulation [55], [56]. Nonetheless, it must be remarked, at once, and in relation to the more rigorous content of the cited references, that the way this validation has been conducted is restricted to a simplified approach, carried out over a large number of sampled designs. Their side effects are shown in terms of the worst cases, enveloping the response to the step commands, as shown in Fig. 7. Each design is defined by generating every sampled model parameter from uniform distributions, whose variation bounds, term by term, are

J_s between −50 % and 50 % of the nominal value of Table 2;

K_b between 75 % and 125 % of a nominal value of 4.5957×10^5 N m^{-1};

θ_{fp} between 0 deg and 1 deg;

C_b conservatively set to zero;

T_{sf} between 0.02 N m and 0.07 N m;

T_{ae} within ±0.25 N m;

K_{ae}, C_{ae} between −100 % and 200 % of their value computed at the highest wind tunnel speed, that is, 50 m s^{-1}. The lower negative bounds aim

at uncertainties against a possible aerodynamic balance that is not considered in the adopted simplified approximation;

T_{rs}, T_{rm} between 0 N m and 0.04 N m;

J_m between 90 % and 110 % of the nominal value of Table 2;

ω_i a conservative current drive bandwidth of 1.0 kHz;

D between 95 % and 100 %, to take into account the possible uncertainty of commands passed to the motor drives;

T_{mf} between 0.07 N m and the maximum value itemized in the controller design paragraph.

It should also be noted that Fig. 7 refers to 40000 simulations, with the displayed nominal positions being not the simulated but the measured ones. In fact, no noticeable change was displayed with respect to sampling just 20000 designs. The results obtained using the PI^{5}PI^0 controller are compared with the worst cases enveloping the response of the standard PID introduced in subsection III-A, which was obtained by simply redesigning the same controller as a PI^{1}PI^0. The comparison shows that the controller with high order integrations provides a smaller aileron position uncertainty band and more accurate position. The results presented here are partially confirmed by the experimental results reported in subsection V-E.

In addition, to avoid clogging the figures, only the lowest and highest orders of the designed PI^{m}PI^{0}s that will be experimentally tested in the following are displayed.

B. PRELIMINARY NUMERICAL/EXPERIMENTAL TUNING

Before analyzing the response of the controlled system to different command signals, preliminary tests were performed to correlate the numerical model. First, contrary

to previous experience [26], [27], there was no apparent benefit from the use of a disturbance observer. Thus, a series of fairly correlated experimental and simulated sine tracking was carried out to understand the reason for missing previously experienced improvements. The motor friction approximately ranging from 0.1 N m to 0.15 N m. Low frequency sine tracking also showed small jumps at the rotation reversals of approximately 0.2 deg at the negative peaks and 0.5 deg at their positive counterparts, which can be related to the free–play recovery, thus confirming the estimated setup value of up to 0.5 deg. Subsequently, based on the numerical/experimental comparison, the conjecture at the base of the chosen disturbance correction was derived. For example, from the experimental tracking of a slow, 1 Hz, sine signal with an amplitude of 5 deg, as shown in Fig. 8, it is possible to see a sample of the associated control torque T_c and observed disturbance T_d, with the resulting torque Δ Torque$= T_c + T_d$, all of which are related to a response with no disturbance correction. While torque control is shown for three m values of PI^{m}PI^0, torque control and the Δ Torque are reported only for PI^{4}PI^0. The other two cases provide similar results. The time histories clearly show that both the PI^{m}PI^0 controller and the disturbance observer identify the same kind of disturbance, being it an average motor friction of about 0.11 N m, so that the mere subtraction of the estimated disturbance will end in just changing the level of T_c, with little effect on Δ Torque. Therefore, given the 10 Hz bandwidth of the PI^{4}PI^0 control and the almost tripled bandwidth of the observer, it becomes plausible that what remains to be compensated is the higher frequency of the displayed resultant Δ Torque. Clearly, this type of compensation can be obtained directly by omitting the term $\mathbf{B}_o$ from (23). Nonetheless, (25) has been preferred for the following reasons. On one hand, the adoption of this disturbance

correction has never been counter–productive and is related to both smooth and slow command, the recorded results associated with a testing without any disturbance correction are almost perfectly identical. On the other hand, while it has provided negligible improvements with smoothly commanded positions, this disturbance correction can be essential in the case of an abrupt saturating command, as will be shown later.

C. NUMERICAL/EXPERIMENTAL CORRELATION

After analyzing the slow response and verifying the free–play, a 30 s long sweep excitation of 5 deg up to 15 Hz was used to identify the frequency response of the complete system and to validate the numerical model. The purpose of this preparatory phase was to understand its effect on the frequency response of all the elements that are not considered in the controller design, such as friction, free–play, and observer.

Referring only to a PI^{4}PI^0 design, Fig. 9 shows the effect of accounting for the existing free–play and plausible friction or the addition of available design options to the basic nominal design, with their use all together. The individual curves are described as follows:

- black: identification of the nominal design (-3 dB bandwidth: 10 Hz);
- light gray: nominal system response after continuous design;
- medium gray: nominal system response after discrete design;
- red: nominal design + disturbance observer + 0.1 N m motor friction + 0.5 deg free–play + $\omega_f = 0.25\,\dot{\theta}_r$ (3 dB bandwidth: 14.4 Hz), leading to a steeper attenuation;
- brown: nominal design + disturbance observer + 0.1 N m motor friction + 0.5 deg free–play (3 dB bandwidth: 13 Hz), leading to a steeper attenuation;
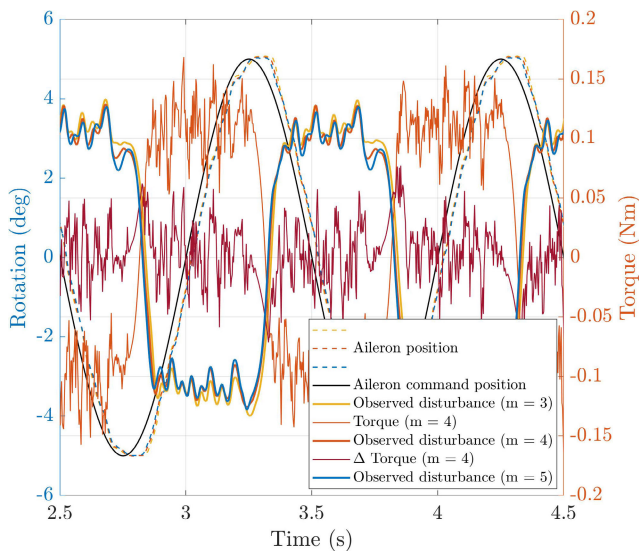

FIGURE 8. Motor torques and observed disturbances due to a 1 Hz, 5 deg sine signal with 0.5 deg free–play, with disturbance correction turned off.
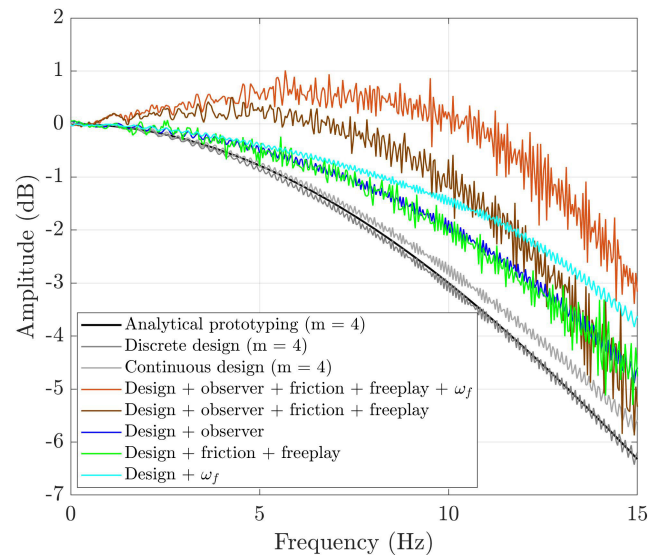

FIGURE 9. Transfer functions from numerical simulations with 0.5 deg free–play.

- blue: nominal design + disturbance observer (3 dB bandwidth: 11.9 Hz);
- green: nominal design + 0.1 N m motor friction + 0.5 deg free–play (3 dB bandwidth: 11.5 Hz);
- cyan: nominal design + $\omega_f = 0.25\,\dot{\theta}_r$ (3 dB bandwidth: 13.3 Hz).

It can be seen that, while any of them results in a widening of the pass–band, neither the existing free–play, nor a plausible friction, nor the results of adding any available single design option to the base nominal design, produce an in–pass–band gain greater than one. A fact that instead happens when all the design options are used together, with a steeper attenuation. Overall, the velocity feed–forward is quite effective in controlling the apparent pass–band, without any further knowledge of the system parameters and without affecting the margins of the nominal design. Furthermore, Fig. 10 simulates the experimental identification of the transfer functions associated with $m = 3 : 5$ and $n = 0$, for a backlash of 0.5 deg. Its experimental counterpart is shown on the left–hand side of Fig. 11. Although not an exact match of the corresponding test results, it provides a fairly acceptable validation of the low–fidelity mathematical model used to anticipate the aileron test bench outcomes. Nonetheless, it should be noted that the simulated transfer function identifications related to a free–play of 1.5 deg are roughly correlated with the right–hand side of Fig. 11, suggesting that a more refined model would be needed for this large free–play.
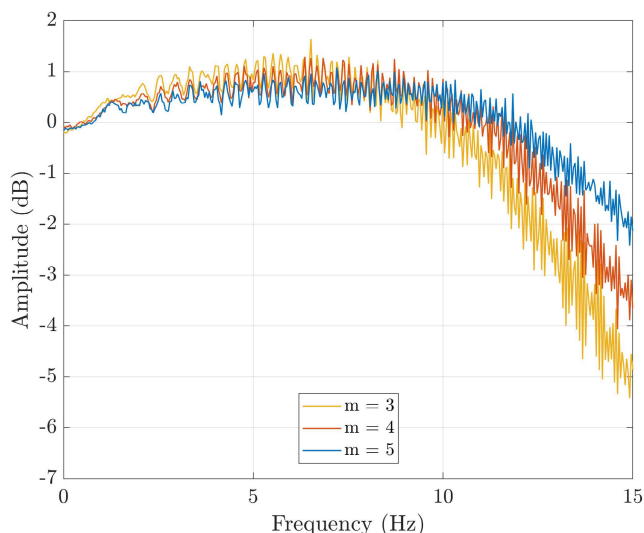

FIGURE 10. Transfer functions from numerical simulations for increasing maximum integration order, with 0.5 deg free–play.

In general, the experimental results show that considering the same design bandwidth, an increase in m leads to an extension of the controller bandwidth in a manner quite similar to the simulated predictions. Moreover, despite the presence of a flexible belt and free–play, the bandwidth was always greater than the design bandwidth. There is also

a small amplification of the response for larger value of free–play (1.5 deg), but it is confined below 1 dB.

Although the related results are not reported in this article, other tests were performed with different combinations of m and n and different values of the design bandwidth. For example, a maximum integration order of 4 was achieved by setting either $m = 4$ and $n = 0$ or $m = 3$ and $n = 1$. Taking into account (4) and (6), without considering the effects of nonlinearities, the reason for choosing the integration order $m = 3, 4, 5$, while setting $n = 0$, is the same as that mentioned in subsection III-A: given the same maximum integration order of the position loop, the ability of the velocity loop to cancel time–varying piecewise polynomial disturbances depends only on the order m. Furthermore, the bandwidth of the velocity loop is generally higher than that of the position loop. Instead, in the experimental tests, the reason for the above choice is that the system has been shown to achieve undesired vibrational behavior sooner when increasing the integration order n instead of m. This is probably owing to the presence of nonlinearities combined with the higher bandwidth of the velocity loop. The design bandwidth was also varied during the tests, which were repeated for $f_0 = 15$ Hz and $f_0 = 20$ Hz. In general, it can be stated that the system is not affected by all these changes, but there appears to be a limit on the maximum integration order, beyond which the system achieves undesired vibrational behavior, depending on the value assigned to the design bandwidth. In fact, when the maximum integration orders are set to $m = 5$ and $n = 0$, the identified transfer functions become somewhat more noisy than their lower m counterparts, and a test cannot be completed for a design bandwidth of 20 Hz, because of the intervention of the current drive thermal image protection. Further comments on these points are provided in the next sub–section.

D. EXPERIMENTAL TESTS
Following what was reported in the previous sub–section, other tests were performed with the disturbance observer turned off and commanding a 0.5 Hz square wave with an amplitude of 10 deg. These tests were carried out to understand from an experimental point of view the importance of using the observer described in subsection II-E and its effects on the system response. Without an observer, the related step responses are rather smooth; however, some disturbances appear in the response, as shown at the top of Fig. 12. The controller could not compensate for disturbances at frequencies higher than the design bandwidth. The amplitude of these disturbances increases as m increases from 3 to 4 and a further increment of m from 4 to 5 seems to make the controller unstable. Analyzing the response of the rotation rates, shown in the middle of Fig. 12, it can be noted that the motor command velocity achieves its maximum value and some oscillations appear around the reference signal in the motor velocity response. For $m = 3$, the amplitude of the oscillation is not relevant when compared with the peak values. However, this issue becomes drastically worse for
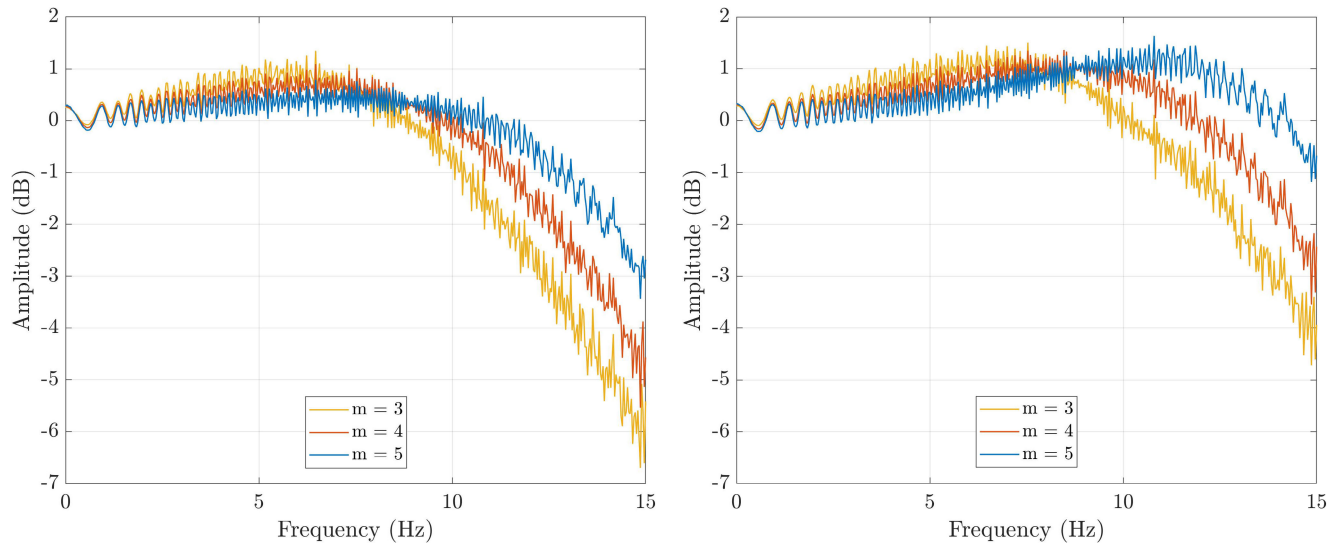
FIGURE 11. Experimental transfer function with 0.5 deg (left) and 1.5 deg (right) free–play.

higher values of m. Thus, for $m = 4$ the oscillations increase in both amplitude and frequency, making the behavior of the servo–actuator extremely jittery.

The results reported at the bottom of Fig. 12 show that after turning off the observer, the motor torque contains oscillations at the same frequency as the velocity signal. However, the amplitude of the oscillations is greater than or equal to one–quarter of the peak value for $m = 3$, drastically worsening from $m = 3$ to $m = 4$. For $m = 4$, the motor torque reaches its saturation, 0.9 N m, and bounces from positive to negative levels. Saturation does not lead to instability, even in the long term. The related behavior is similar to that of a bang–bang controller with an unacceptable chattering response. For $m = 5$, the effect is the same but stronger, so the current overload protection functions are embedded into the drive trips after a few seconds, stopping the motor.

The same tests were repeated after the observer turned off. They confirmed that the use of the disturbance observer described in subsection II-E can significantly improve the PI^{3}PI^0 and PI^{4}PI^0 controller responses, whereas it is essential when the maximum integration order is greater than 4. Analyzing the response in terms of the rotation rate and torque, all cases from $m = 3$ to $m = 5$ do not show response criticalities. Looking at the rotation rate, shown on the left side of Fig. 13, it can be noted that although the motor command velocity achieves its maximum value, the controller compensates for the effects of the rate saturation and no oscillation appears. The motor velocity signal was clean and showed no signs of disturbances or noise. It can thus be seen that the observer completely removes disturbances at frequencies higher than the design bandwidth and at increasing values of m. Moreover, the results reported on the right side of Fig. 13 show that the motor torque response is very clean and never reaches saturation. Therefore, the comparison between the square wave response, with and

without the disturbance observer, supports the need to use this correction in the case of abrupt commands and demonstrates the correctness of the conjecture at the base of the chosen disturbance correction, as mentioned in subsection V-B.

The same square wave was used to assess the response of the working free–play of 0.5 deg against that close to the ratcheting bound of 1.5 deg, as shown in Fig. 14. Looking at the experimental response, it can be noted that the system approached the reference position faster than a critically damped system, almost completely limiting the overshoot and, at the same time, accurately maintaining the desired position. When m increases, the step response gradually improves, and for $m = 5$, the already small overshoot becomes almost entirely negligible. This improvement adds to the ability of the proposed system to counteract external disturbances and compensate for the perturbations in the model parameters described in subsection V-A. Moreover, these experimental results demonstrate that the closed loop system seems quite insensitive to belt tension changes that determine the free–play size, except for the small settling oscillations of the (1.5 deg) free–play, because to the belt slack side is close to causing tooth jumping.

The response using high order integrations is then compared with the response using the simple dual loop PID controller, which has already been adopted for comparison purposes in subsection V-A. Based on what is explained in subsection III-A, the PID was obtained by redesigning the controller as a PI^{1}PI^0, which was tested in its standard form, that is, with the same amount of feed–forward ω_f, with a 0.5 deg free–play. Therefore, after using high order controllers, the same tests were repeated under the same conditions, with $m = 1$. The results show that the same target, achieved using high order integrations, was not achieved by the dual loop PID controller, except for oscillations of amplitude corresponding to the 0.5 deg free–play around
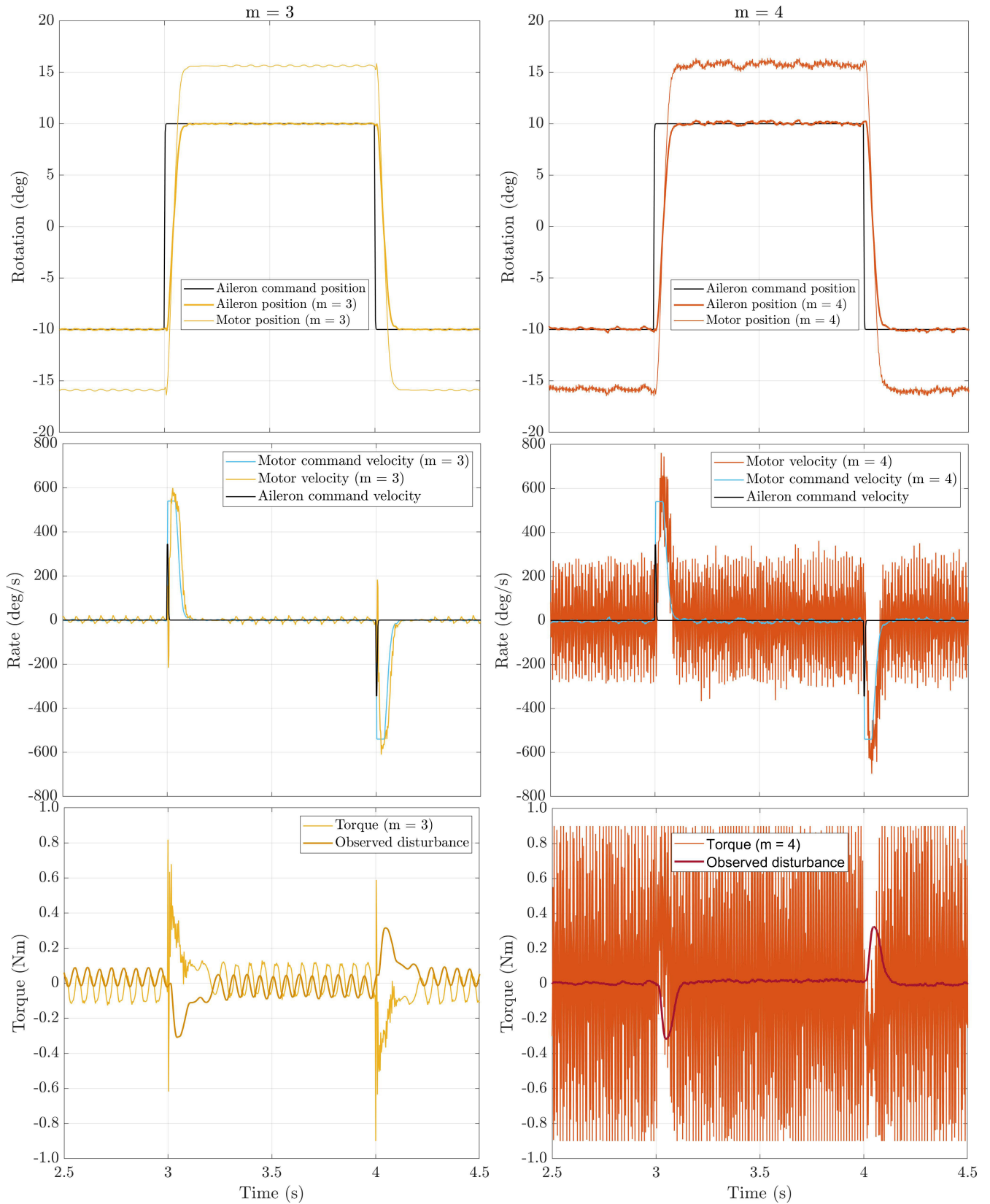
FIGURE 12. Experimental tracking of square wave signal after turning off the disturbance observer, with 0.5 deg free–play, for two maximum integration order of the velocity loop: *m* = 3 (left) and *m* = 4 (right).
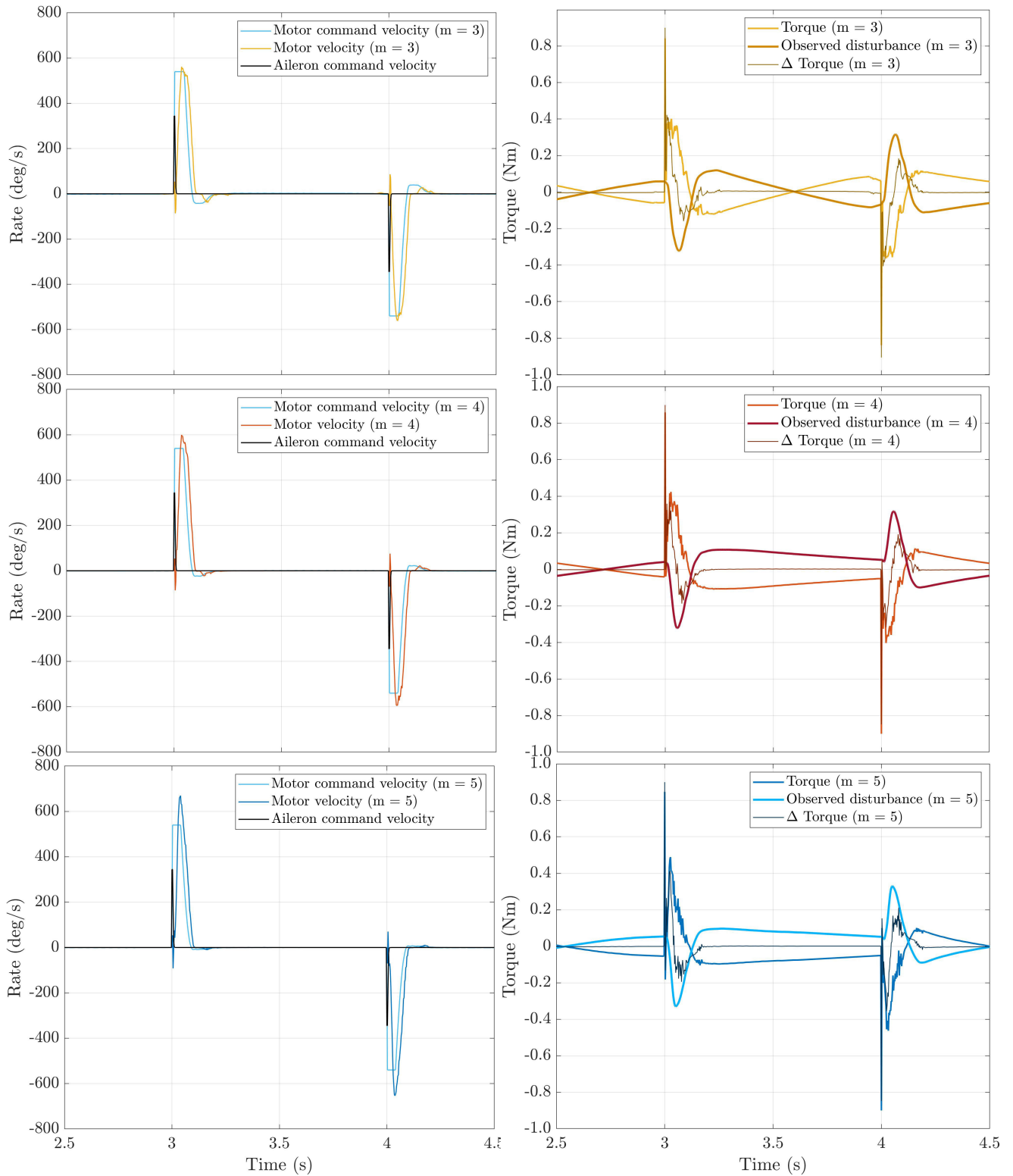
FIGURE 13. Motor rotation rate (left) and torque (right) corresponding to the square wave signal tracking of Fig. 14, for increasing maximum integration order of the velocity loop: $m = 3$, $m = 4$ and $m = 5$.

the reference position. This confirms the effectiveness of the controller based on high order integrations, with the additional 1.5 deg free–play being much higher than the variations considered during the Monte Carlo simulations.

In conclusion, the only limitation of the proposed method is the constraint on the maximum integration order as a function of the design bandwidth. It is not possible to increase the integration order equally for any system or design bandwidth
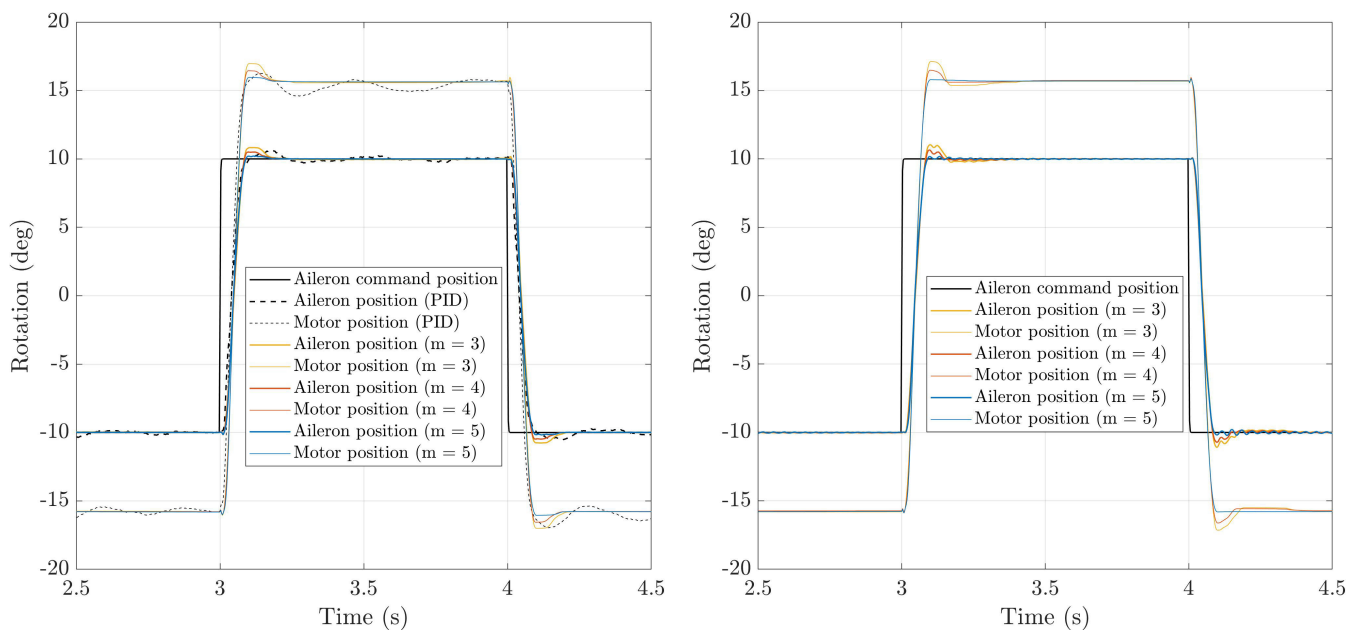
FIGURE 14. Experimental tracking of square wave signal after turning on the disturbance observer, with 0.5 deg (left) and 1.5 deg (right) free–play.

value. In the specific case of this study, by increasing the bandwidth from 10 Hz to 20 Hz, the controller response worsens for $m = 5$, as when the observer is turned off.

E. TWO FURTHER TESTS AGAINST SIGNIFICANT OFF–DESIGN CONDITIONS

A first further test was performed to evaluate the effect of high order integration when using only the aileron encoder and by setting $\theta = \tau \theta_s$, instead of reading the motor encoder and without changing anything else in the existing dual sensor implementation. Clearly, the alternative method of relying only on the motor encoder is of little use. In fact, the substantial co–location of the encoder and torque makes it easy to position the motor without recovering any free–play and/or elastic displacement in the position loop. Therefore, the previously used square wave command test was repeated to verify the behavior associated with the use of only the nonco–located aileron encoder. As shown in Fig. 15, increasing the integration order allows the controller to become better and better capable of compensating a free–play–related limit cycle caused by abrupt commanded position changes. For $m = 3$, the limit cycle has an amplitude corresponding to full free–play. Then, by increasing the integration order up to $m = 4$, the overshoot decreases, and the response settles to the commanded position after a smaller counter oscillation. Eventually, for $m = 5$, the response further improves, becoming significantly similar to that obtained using the two encoders. Despite the free–play and reduced transmission stiffness due to the constrained belt tension, the above result is aided by the separation of the control pass band against the no–free–play motor–aileron vibration mode.
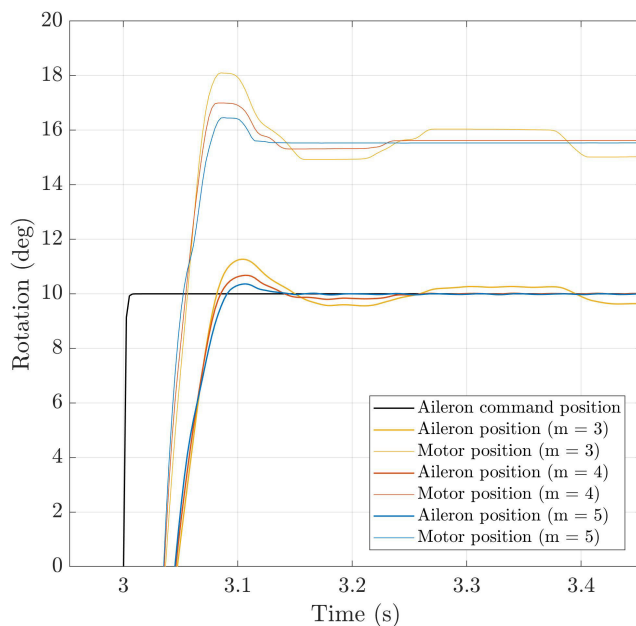

FIGURE 15. Experimental tracking of square wave signal using only the aileron encoder (with 0.5 deg free–play).

It should also be noted that, with just a 0.5 deg free–play, the simple dual loop PID design, which provided an acceptable response with two encoders, limited cycling with free–play hunting oscillations.

Moreover, in contrast to the two encoder implementations, all the above integration orders were unstable, with a free–play of 1.5 deg. Therefore, even if sensing the position at the load can provide a fairly acceptable solution with an appropriate high order integration, the design freedom caused by the use of two encoders should be preferred.

Another test was conducted to further demonstrate the tracking capability of the controller, after significantly changing the operating conditions and test setup. A mass of 100 g was added to the aileron by placing its center of gravity at 8 cm from its hinge. The aileron was mounted in an inverted pendulum configuration, which made it statically unstable with a small right–plane pole. To make it easier for a possible sustained instability compared to previous test cases, the amplitude of the square wave was doubled to amplify the effect of the sharp velocity–torque saturations and the related windup recovery. The modified test bench configuration is shown in Fig. 16. The aluminum mass added at the trailing edge of the aileron makes its moment of inertia $J_s = 7.19 \times 10^{-4}\,\mathrm{kg\,m^2}$, which is almost an order of magnitude greater than its true value. The response to the 20 deg square wave signal is shown in Fig. 17. Despite
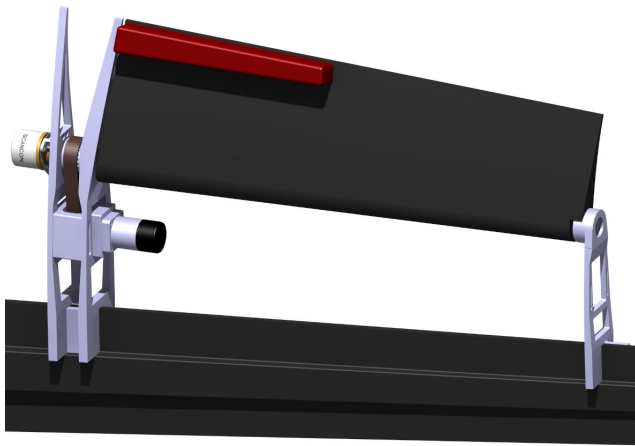

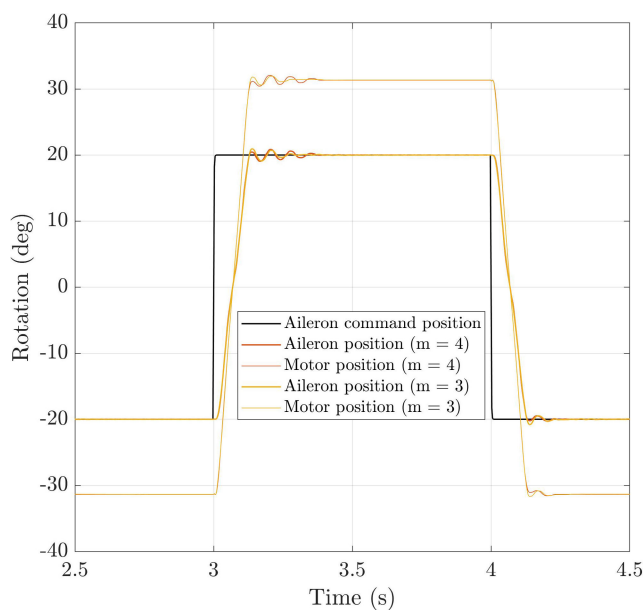**FIGURE 16.** Aileron test bench configuration with added mass.

FIGURE 17. Experimental tracking of square wave signal with added mass, in the inverted pendulum configuration (0.5 deg free–play).

a 2.35 times change with respect to the nominal design inertia J, combined with a slight open loop instability, the controller is capable of accurately tracking sudden repeated aileron commands. The initial oscillations are due to the loss of damping caused by bringing the open loop velocity gain close to its corresponding stability margin, which makes it more difficult to recover a steady 20 deg free–play. No test for a fifth order integral has been reported, because the few attempts ended in sustained and dangerous belt ratcheting, which could only be cured by lowering the design bandwidth.

VI. CONCLUSION

To improve the performance of a servo–actuation system commanding the rotation of a control surface, this study presented the formulation of a dual loop velocity/position controller using arbitrary high order integrations. Owing to the adoption of high order integrations, combined with a simple yet effective anti windup compensation scheme, the aforesaid controller was capable of tolerating uncertain design parameters and time–varying disturbances. This intrinsic capability allowes such a controller to be suitably designed using a simple pole–placement method, where the controller is associated with a simplified model of the system to be controlled. This model does not require knowledge of many significant terms, such as nonlinearities, saturations, integrator windup, the use of two sensors, compliant transmission with possible free–plays, and sliding friction. A further rejection of higher–frequency disturbances, not suppressed by the integral terms, was made possible by the adoption of a specialized disturbance observer. Both the high order integration controller, disturbance observer, and anti–windup were cast and designed in a unified continuous time state form and then digitized with a zero–order hold conversion.

The design method was applied to the test bench of an aileron installed on an aeroelastic wind tunnel model and actuated by an electric motor through a toothed belt drive. Because of the need to emulate the saturation constraints of the corresponding full–scale actuation system, both the aileron and motor are equipped with a position encoder that makes the dual loop controller necessary.

After the design, the controller was connected to another numerical model that was more detailed than the simplified model used during the linear design, which allowed the consideration of the most significant linear and nonlinear terms affecting the performance of the system. The second model was used to perform an uncertainty propagation study based on Monte Carlo simulations over a very large number of randomly sampled designs. This phase shows the effectiveness and advantages of the proposed control strategy against design uncertainties, external disturbances, and model–reality mismatches compared to the same study carried out on a traditional servo–controller adopting only one integral term.

The simulations were followed by a numerical/experimental correlation and several experimental tests on

specific high order integration controllers. The experimental tests demonstrated the need, and therefore, the effectiveness of the proposed observer to be used in combination with high order integration. The efficacy of the developed technique was demonstrated by overall verification of the attainment of good responses to basic step–like commands, which were also compared with the behavior of the considered traditional controller. More specific and successful tests showed the controller's ability to work despite significant changes to the test rig configuration, such as free–plays owing to insufficient belt tensioning and large mass changes, far greater than the already large changes introduced during Monte Carlo simulations. Moreover, the controller has shown that it can work even using only encoders mounted on the aileron side. The results of this test are significant because they directly show that increasing the integration order improves the accuracy of the controller response.

Future work will focus on the application of high order integration controllers to the control of morphing aeronautical structures in which the superposition of aerodynamic shape variations and the elastic forces due to the commanded deformation require large changes in the control effort; the control of free–play induced Limit Cycle Oscillations (LCO) of control surfaces installed on the T–tail of an aeroelastic wind tunnel model.

REFERENCES

[1] T. L. Lomax, *Structural Loads Analysis for Commercial Transport Aircraft*. Reston, Virginia, USA: AIAA Inc., 1996.

[2] J. R. Wright and J. E. Cooper, *Introduction to Aircraft Aeroelasticity and Loads*. Hoboken, NJ, USA: Wiley, 2007.

[3] S. Ricci, A. Scotti, and D. Zanotti, "Control of an all-movable foreplane for a three surfaces aircraft wind tunnel model," *Mech. Syst. Signal Process.*, vol. 20, no. 5, pp. 1044–1066, Jul. 2006.

[4] A. De Gaspari, S. Ricci, L. Riccobene, and A. Scotti, "Active aeroelastic control over a multi-surface wing: Modelling and wind tunnel testing," *AIAA J.*, vol. 47, no. 9, pp. 1995–2010, Sep. 2009.

[5] K. H. Ang, G. Chong, and Y. Li, "PID control system analysis, design, and technology," *IEEE Trans. Control Syst. Technol.*, vol. 13, no. 4, pp. 559–576, 2005.

[6] A. O'Dwyer, *Handbook of PI and PID Controller Tuning Rules*. Singapore: World Scientific Publishing Co., 2009.

[7] H. Habibi, H. Rahimi Nohooji, and I. Howard, "Adaptive PID control of wind turbines for power regulation with unknown control direction and actuator faults," *IEEE Access*, vol. 6, pp. 37464–37479, 2018.

[8] G. Huang and W. Lin, "Design of adaptive PID control system based on embedded device," in *Proc. IEEE 3rd Adv. Inf. Manage., Communicates, Electron. Autom. Control Conf. (IMCEC)*, Oct. 2019, pp. 1530–1533.

[9] P. Gao, G. Zhang, H. Ouyang, and L. Mei, "An adaptive super twisting nonlinear fractional order PID sliding mode control of permanent magnet synchronous motor speed regulation system based on extended state observer," *IEEE Access*, vol. 8, pp. 53498–53510, 2020.

[10] Y. D. Mfoumboulou, "Design of a model reference adaptive PID control algorithm for a tank system," *Int. J. Electr. Comput. Eng. (IJECE)*, vol. 11, no. 1, p. 300, Feb. 2021.

[11] P.-J. Ko and M.-C. Tsai, "H∞ control design of PID-like controller for speed drive systems," *IEEE Access*, vol. 6, pp. 36711–36722, 2018.

[12] B. Hekimoglu, "Optimal tuning of fractional order PID controller for DC motor speed control via chaotic atom search optimization algorithm," *IEEE Access*, vol. 7, pp. 38100–38114, 2019.

[13] M. F. D. Santos, A. F. D. S. Neto, L. De Mello Honório, M. F. Da Silva, and P. Mercorelli, "Robust and optimal control designed for autonomous surface vessel prototypes," *IEEE Access*, vol. 11, pp. 9597–9612, 2023.

[14] M. Ahmadi Kamarposhti, H. Shokouhandeh, M. Alipur, I. Colak, H. Zare, and K. Eguchi, "Optimal designing of fuzzy-PID controller in the load-frequency control loop of hydro-thermal power system connected to wind farm by HVDC lines," *IEEE Access*, vol. 10, pp. 63812–63822, 2022.

[15] Z. Zhu, Y. Liu, Y. He, W. Wu, H. Wang, C. Huang, and B. Ye, "Fuzzy PID control of the three-degree-of-freedom parallel mechanism based on genetic algorithm," *Appl. Sci.*, vol. 12, no. 21, p. 11128, Nov. 2022.

[16] G. M. Scott, J. W. Shavlik, and W. H. Ray, "Refining PID controllers using neural networks," *Neural Comput.*, vol. 4, no. 5, pp. 746–757, Sep. 1992.

[17] R. Hernández-Alvarado, L. García-Valdovinos, T. Salgado-Jiménez, A. Gómez-Espinosa, and F. Fonseca-Navarro, "Neural network-based self-tuning PID control for underwater vehicles," *Sensors*, vol. 16, no. 9, p. 1429, Sep. 2016.

[18] C. B. Jabeur and H. Seddik, "Optimized neural networks-PID controller with wind rejection strategy for a quad-rotor," *J. Robot. Control (JRC)*, vol. 3, no. 1, pp. 62–72, Oct. 2021.

[19] M. Manetti, M. Morandini, and P. Mantegazza, "Self-tuning shape control of massively actuated adaptive mirrors," *IEEE Trans. Control Syst. Technol.*, vol. 22, no. 3, pp. 838–852, May 2014.

[20] J. Li and W. Li, "On-line PID parameters optimization control for wind power generation system based on genetic algorithm," *IEEE Access*, vol. 8, pp. 137094–137100, 2020.

[21] A. San-Millan, V. Feliu-Batlle, and S. S. Aphale, "Two-degrees-of-freedom PI2D controller for precise nanopositioning in the presence of hardware-induced constant time delay," *ISA Trans.*, vol. 91, pp. 207–217, Aug. 2019.

[22] A. A. Eielsen, M. Burger, J. T. Gravdahl, and K. Y. Pettersen, "PI2-controller applied to a piezoelectric nanopositioner using conditional integrators and optimal tuning," *IFAC Proc. Volumes*, vol. 44, no. 1, pp. 887–892, Jan. 2011.

[23] I. Rusnak, "Family of the PID controllers," in *Introduction To PID Controllers—Theory, Tuning and Application To Frontier Areas*. London, U.K.: IntechOpen, 2012, ch. 2, pp. 31–48.

[24] *DIGIVEX μmicro Drive Digital Servoamplifier—User and Commissioning Manual*, Hannifin Corp., Cleveland, OH, USA, 2004.

[25] S. Seshagiri and H. K. Khalil, "Robust output feedback regulation of minimum-phase nonlinear systems using conditional integrators," *Automatica*, vol. 41, no. 1, pp. 43–54, Jan. 2005.

[26] A. De Gaspari, A. Mannarino, and P. Mantegazza, "A dual loop strategy for the design of a control surface actuation system with nonlinear limitations," *Mech. Syst. Signal Process.*, vol. 90, pp. 334–349, Jun. 2017.

[27] A. De Gaspari, F. Toffol, P. Mantegazza, and A. Mannarino, "Optimal and robust design of a control surface actuation system within the GLAMOUR project," *Aerotecnica Missili Spazio*, vol. 95, no. 4, pp. 219–231, Oct. 2016.

[28] S. Habibi, J. Roach, and G. Luecke, "Inner-loop control for electromechanical (EMA) flight surface actuation systems," *J. Dyn. Syst., Meas., Control*, vol. 130, no. 5, pp. 1–13, Sep. 2008.

[29] N. Fonzi, S. Ricci, and E. Livne, "Numerical and experimental investigations on freeplay–based LCO phenomena on a T–tail model," in *Proc. AIAA Scitech. Forum*, San Diego, CA, USA, 2022, pp. 1–20.

[30] S. Ricci, A. De Gaspari, L. Riccobene, and F. Fonte, "Design and wind tunnel test validation of gust load alleviation systems," in *Proc. 58th AIAA/ASCE/AHS/ASC Struct., Structural Dyn., Mater. Conf.*, Jan. 2017, pp. 1–12.

[31] R. M. Phelan, *Automatic Control Systems*. Ithaca, NY, USA: Cornell University Press, 1977.

[32] M. Ruth, K. Lebsock, and C. Dennehy, "What's new is what's old: Use of bode's integral theorem (circa 1945) to provide insight for 21st century spacecraft attitude control system design tuning," in *Proc. AIAA Guid., Navigat., Control Conf.*, Aug. 2010, pp. 1–26.

[33] G. Stein, "Respect the unstable," *IEEE Control Syst. Mag.*, vol. 23, no. 4, pp. 12–25, Aug. 2003.

[34] K. J. Åström and R. M. Murray, *Feedback Systems: An Introduction for Scientists and Engineers*. Princeton, NJ, USA: Princeton Univ. Press, 2020.

[35] K. Johan Astrom and L. Rundqwist, "Integrator windup and how to avoid it," in *Proc. Amer. Control Conf.*, Jun. 1989, pp. 1693–1698.

[36] K. J. Åström and B. Wittenmark, *Computer–Controlled Systems: Theory and Design*, 3rd ed. New York, NY, USA: Dover, 2011.

[37] Wikipedia Contributors. (2024). *Butterworth filter—Wikipedia, The Free Encyclopedia*. [Online]. Available: https://en.wikipedia.org/w/index.php?title=Butterworth_filter&oldid=1195597266

[38] S. Galeani, S. Tarbouriech, M. Turner, and L. Zaccarian, "A tutorial on modern anti-windup design," *Eur. J. Control*, vol. 15, nos. 3–4, pp. 418–440, Jan. 2009.

[39] A. Radke and Z. Gao, "A survey of state and disturbance observers for practitioners," in *Proc. Amer. Control Conf.*, 2006, pp. 5183–5188.

[40] G. F. Franklin, J. D. Powell, and M. Workman, *Digital Control of Dynamic Systems*. Half Moon Bay, CA, USA: Ellis–Kagle Press, 2010.

[41] C. D. Johnson, "Theory of disturbance—Accommodating controllers," *Control Dyn. Syst.*, vol. 12, pp. 387–489, Jul. 1976.

[42] C. D. Johnson, "Real-time disturbance-observers; origin and evolution of the idea part 1: The early years," in *Proc. 40th Southeastern Symp. Syst. Theory (SSST)*, Mar. 2008, pp. 88–91.

[43] G. Herbst, "A simulative study on active disturbance rejection control (ADRC) as a control tool for practitioners," *Electronics*, vol. 2, no. 4, pp. 246–279, Aug. 2013.

[44] S. Shi, Z. Zeng, C. Zhao, L. Guo, and P. Chen, "Improved active disturbance rejection control (ADRC) with extended state filters," *Energies*, vol. 15, no. 16, p. 5799, Aug. 2022.

[45] B. N. Datta, *Numerical Methods for Linear Control Systems Design and Analysis*. Amsterdam, The Netherlands: Elsevier, 2004.

[46] K. J. Åström, "Practical aspects on digital implementation of control laws," in *Computer–Aided Design and Analysis of Digital Guidance and Control Systems*. Essex, U.K.: Neully sur Seine, 1983, p. 9.

[47] R. Petrella, M. Tursini, L. Peretti, and M. Zigliotto, "Speed measurement algorithms for low-resolution incremental encoder equipped drives: A comparative analysis," in *Proc. Int. Aegean Conf. Electr. Mach. Power Electron.*, Sep. 2007, pp. 780–787.

[48] Texas Instrum. (2020). *Tech. Reference Manual; TMS320x2833x, TMS320x2823x*. [Online]. Available: https://www.ti.com/lit/ug/spruip07/spruip07.pdf

[49] G. Liu, "On velocity estimation using position measurements," in *Proc. Amer. Control Conf.*, Anchorage, AK, USA, May 2002, pp. 1115–1120.

[50] Harmon. Drive. (2022). *AC Servo Actuator—RSF Supermini Ser. Manual*. [Online]. Available: https://harmonicdrive.de/fileadmin/user_upload/2015_06_ED_1019818_RSFmini.pdf

[51] I. P. S. Skogestad, *Multivariable Feedback Control, Analysis and Design*. Hoboken, NJ, USA: Wiley, 2008.

[52] M. Šebek and Z. Hurák, "An often missed detail: Formula relating peek sensitivity with gain margin less than one," in *Proc. 17th Int. Conf. Process Control*, 2009, pp. 65–72.

[53] S. Ricci, F. Toffol, L. Marchetti, A. De Gaspari, J. V. Chardi, L. Riccobene, F. Fonte, and P. Mantegazza, "Design and experimental validation of gust load alleviation systems based on static output feedback," in *Proc. AIAA SciTech Forum*, San Diego, CA, USA, Jan. 2022, pp. 3–7.

[54] RTAI—The Real Time Appl. Interface for Linux. (2021). *Department of Aerospace Science and Technology (DAER)*. [Online]. Available: https://www.rtai.org/?Homepage

[55] R. F. Stengel, L. R. Ray, and C. I. Marrison, "Probabilistic evaluation of control system robustness," *Int. J. Syst. Sci.*, vol. 26, no. 7, pp. 1363–1382, Jul. 1995.

[56] Q. Wang and R. F. Stengel, "Robust control of nonlinear systems with parametric uncertainty," *Automatica*, vol. 38, no. 9, pp. 1591–1599, Sep. 2002.

ALESSANDRO DE GASPARI received the M.S. and Ph.D. degrees in aerospace engineering from Politecnico di Milano, Milan, Italy, in 2006 and 2011, respectively.

From 2011 to 2017, he was a Postdoctoral Research Fellow. He became an Assistant Professor and an Associate Professor with Politecnico di Milano, in 2017 and 2023, respectively. His current research interests include structural dynamics, design optimization, morphing aircraft, wind tunnel testing, aeroelasticity, and active control of aerospace structures.
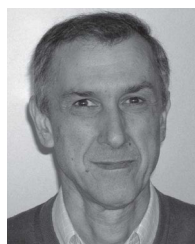
PAOLO MANTEGAZZA received the degree in aeronautical engineering from Politecnico di Milano, Italy, in 1972.

He became an Assistant Professor, an Associate Professor, and a Full Professor with Politecnico di Milano, in 1976, 1982, and 1992, respectively. He taught courses related to the dynamics and control of aerospace structures and aeroservoelasticity. His research interests include structural dynamics, aeroservoelasticity, active control of structures, and aeroelastic systems.

• • •